Remote Sensing of Environment 322 (2025) 114705

Contents lists available at ScienceDirect

Remote Sensing of Environment

journal homepage: www.elsevier.com/locate/rse

# Urban thermal anisotropies by local climate zones: An assessment using multi-angle land surface temperatures from ECOSTRESS

Yue Chang [a,b], Qihao Weng [a,b,c,*], James A. Voogt [d], Jingfeng Xiao [e]

[a] JC STEM Lab of Earth Observations, Department of Land Surveying and Geo-Informatics, The Hong Kong Polytechnic University, Kowloon, Hong Kong, China
[b] Research Centre for Artificial Intelligence in Geomatics, The Hong Kong Polytechnic University, Kowloon, Hong Kong, China
[c] Research Institute for Land and Space, The Hong Kong Polytechnic University, Hung Hom, Hong Kong, China
[d] Department of Geography and Environment, Faculty of Social Science, University of Western Ontario, London, ON, Canada
[e] Earth Systems Research Center, Institute for the Study of Earth, Oceans, and Space, University of New Hampshire, Durham, NH, USA

ARTICLE INFO

Edited by Jing M. Chen

*Keywords:*
Land surface temperature
Urban thermal anisotropy
ECOSTRESS
Diurnal directional effects
Local climate zones
Urban areas
Surface urban heat island

ABSTRACT

Knowledge of anisotropy-induced spatial and temporal variations of land surface temperature (LST) is crucial for enhancing the quality of remote sensing products, refining land surface process modeling, and optimizing climate models. However, the limited availability of simultaneous multi-angle LST observations from space has hindered the exploration of this topic. NASA's latest ECOSTRESS sensor deployed on the International Space Station (ISS) generates multi-angle LST measurements at a 70-m spatial resolution for different times of day/night, providing a new avenue for investigating urban thermal anisotropy. In this study, we presented an initial examination of the performance of ECOSTRESS LST observations in unraveling the fine-grained urban thermal anisotropy, by taking the City of Phoenix, Arizona, United States, as the study area. We proposed a method to generate a quasi-simultaneous multi-angle ECOSTRESS LST dataset over the course of the diurnal cycle with the assistance of air temperature data from weather stations and hourly LST observations from a geostationary satellite, GOES-R. We then examined the thermal anisotropic patterns and their diurnal and seasonal variations across different Local Climate Zones (LCZs) at a spatial resolution of 200 m. Based on quasi-simultaneous multi-angle ECOSTRESS observations, Vinnikov and Vinnikov-RL models were employed to generate LCZ-scale anisotropy profiles of the study area to quantify and correct the LST directional effect. The results revealed that ECOSTRESS observations manifest unique angular patterns, featuring substantial variations in sensor viewing azimuth angles (VAA) and limited changes in sensor viewing zenith angles (VZA) within a 30° range. The angular effect led to notable variations in the observed LST, with potential deviations at the city scale of up to 10 K during winter and around 5 K during summer, relative to the nadir LST. Furthermore, the LST anisotropy exhibited distinct diurnal and seasonal patterns across LCZs, characterized by prominent variations in the intensity and width of hot/cold spots. LCZ 6, 9, and D typically displayed higher hotspot intensity and width than other LCZs at varying times of day in both summer and winter. In addition, the Vinnikov-RL model had good performance in simulating diurnal LST anisotropy over LCZs. This study reveals the potential of multi-angle ECOSTRESS LST observations in exploring urban thermal anisotropy, and contributes to better utilization of ECOSTRESS LST products. The integration of ECOSTRESS LST data with other satellite derived LST data have important implications for studying urban climate and improving long-term surface climate record, contributing to global climate studies.

## 1. Introduction

Land surface temperature (LST) serves as a key parameter in characterizing the hydrothermal processes on the Earth's surface (Manoli et al., 2020; Schwaab et al., 2021; Su et al., 2023). Existing satellite thermal remote sensing systems offer an effective approach to obtaining LST measurements with different spatiotemporal resolutions from local to global scales (Li et al., 2023; Weng, 2009). These multi-decadal records find widespread applications in various studies including climate change simulation, evapotranspiration estimation, vegetation drought

* Corresponding author at: JC STEM Lab of Earth Observations, Department of Land Surveying and Geo-Informatics, The Hong Kong Polytechnic University, Kowloon, Hong Kong, China.
*E-mail address:* qihao.weng@polyu.edu.hk (Q. Weng).

https://doi.org/10.1016/j.rse.2025.114705
Received 2 January 2024; Received in revised form 24 February 2025; Accepted 7 March 2025
Available online 15 March 2025

monitoring, and urban heat stress assessment, significantly contributing to the advancement of knowledge in the relevant domains (Hulley et al., 2019; Jiao et al., 2021; Wooster et al., 2021; Xia et al., 2022). With the continuous acquisition of LST observations from space, synergistic utilization of multi-satellite data becomes particularly crucial in collectively addressing the future challenges of global warming and seeking viable solutions.

The main challenges to the multi-satellite LST integration include diurnal cycle (i.e., the variations of observation times), cloud contamination and angular anisotropy (Fu et al., 2019; Vinnikov et al., 2012; Wang et al., 2022a). Angular anisotropy refers to the reliance of satellite LST observations on sensor view angles including azimuth and zenith angles (Voogt, 2008). It has been examined over diverse surfaces encompassing cropland, forest, bare soil, and urban areas (Guillevic et al., 2013; Hu et al., 2023; Wang et al., 2023). Previous studies have reported that temperature disparities resulting from angular anisotropy can reach 14 K on a winter day and 9 K on a summer day over densely urbanized areas (Lagouarde and Irvine, 2008; Voogt and Oke, 1998). On natural surfaces with continuously homogeneous canopy, directional temperature variability is relatively small, typically below 2 K (Rasmussen et al., 2011). Satellite-derived LST observations are limited to representing the thermal status of specific facets of the target (Stewart et al., 2021). Accordingly, variations in sensor viewing geometry can introduce directional biases in LST measurements, particularly in highly heterogeneous urban environments with intricate 3D structures and materials (Du et al., 2023). Therefore, knowledge on LST anisotropy is required not only for ensuring the accurate measurement and comparability of multi-source LST products but also for bolstering confidence in their practical applications.

Five types of models have been developed for characterizing and simulating thermal radiation directionality (TRD), namely, parametric models (or semi-physical kernel-driven models), 3D models, hybrid models, geometric optical modes and radiative transfer models (Bian et al., 2018; Cao et al., 2019; Lagouarde and Irvine, 2008). These models, combined with multi-angle LST datasets obtained from laboratory experiments, in-situ measurements, airborne observations and space-borne observations, have greatly enhanced our comprehension of the anisotropic impacts on LST interpretation (Jiang et al., 2022; Qin et al., 2023; Wang et al., 2021). Nonetheless, fine spatiotemporal characteristics of urban thermal anisotropy at the scale of satellite observations remain unclear. Physical models usually require many parameters for inputs, such as landscape structural information and component temperature, making them better suited for experimental/modeling data sets than for satellite data (Duffour et al., 2015; Guo et al., 2019). The kernel-driven models, however, are designed to estimate and correct the remotely sensed LST directionality (Jiang et al., 2021; Vinnikov et al., 2012). With only three or four unknown parameters, the kernel models generally strike a favorable tradeoff between physical representation, accuracy and practicality (Ermida et al., 2017). For the visible and near-infrared spectra, the kernel-driven models have been widely employed in combined use of geostationary and polar-orbiting satellites derived reflectance/albedo products (Lagouarde and Irvine, 2008; Roujean, 2000). In recent years, several studies have assessed the performance of different kernel-driven models, offering new evidence for their practical potential in harmonizing LST products derived from different sensors (Cao et al., 2021; Ermida et al., 2018). However, it is worth noting that existing kernel-driven models rely on multi-angle LST observations acquired simultaneously to solve the unknowns. Obtaining synchronous multi-angle observations from ground and airborne measurements is straightforward, but it poses greater challenges to satellite observations (Bian et al., 2021; Hu et al., 2016). Limited availability of simultaneous or quasi-simultaneous multi-angle LST datasets has hindered further exploration of fine spatiotemporal variations in urban thermal anisotropy at the satellite observing scale through kernel-driven modeling approaches.

The recently launched ECOSTRESS sensor by NASA's Jet Propulsion Laboratory (JPL) is opening a new path for the exploration of fine-scale spatial and temporal patterns in urban LST anisotropy. Installed on the International Space Station (ISS) in July 2018, ECOSTRESS swiftly initiated the acquisition of thermal infrared (TIR) data with the native spatial resolution of 38 m by 69 m (Hulley et al., 2019). The ISS maintains a precessing orbit, enabling ECOSTRESS to possess diurnal sampling capability globally (between ~52 degrees North and ~ 52 degrees South). Additionally, it provides more frequent revisits, with intervals of three to five days depending on latitude and time of year. Each ECOSTRESS image scene covers a swath width of about 400 km and is captured in approximately 52 s at various times throughout the diurnal cycle (Chang et al., 2023). ECOSTRESS is equipped with five TIR bands for more accurate LST retrievals over urban areas (Hulley et al., 2021). Besides, analysis of the first-level geolocation product reveals pronounced variability in sensor viewing azimuth angles (VAA) for ECOSTRESS LST observations, spanning from 0 to 360 degrees, while the sensor viewing zenith angles (VZA) remains within a range of 30 degrees. Many studies based on satellite observations, unmanned aerial vehicle (UAV) measurements, and simulation data have demonstrated that LST can exhibit significant variations with changes in sensor VAA, particularly during daytime with intense incoming solar radiation (Hu and Wendel, 2019; Hu et al., 2023; Jiang et al., 2022; Lagouarde et al., 2010; Wang et al., 2021). For instance, a recent UAV-based study conducted over a residential area (classified as open midrise buildings, LCZ5) revealed that at 13:10 local time, changes in sensor VAA could result in LST differences of up to 6.6 °C at a constant sensor VZA of 15 degrees and up to 8.2 °C at a constant sensor VZA of 30 degrees (Jiang et al., 2022). Scale effects and variations in sun-sensor geometry modify the proportions of illuminated and shaded surface components, thus substantially impacting LST anisotropy. However, due to the inherent observation geometry of traditional satellites, most existing spaceborne studies focus primarily on LST anisotropy variations caused by changes in sensor VZA. In this context, the distinctive observation characteristics of ECOSTRESS present a valuable opportunity to advance our comprehensive understanding of LST anisotropy.

Currently, the main data sources for satellite-scale LST anisotropy studies are the single sensor source capable of generating multi-angular observations, such as MODIS and ASTER series, and the multiple remotely sensed sources with varying view geometries, such as coupling polar-orbiting and/or geostationary (i.e., GOES and MSG series) satellites (Coll et al., 2019; Ermida et al., 2018; Guillevic et al., 2013; Wang et al., 2022b). Spatially, LST products derived from these polar-orbiting/geostationary satellites have a 1-km resolution or coarser, which cannot adequately capture the spatial heterogeneity of urban thermal environments. As a result, existing satellite-based studies focus primarily on LST anisotropic analysis at 1-km grid or a city in entirety. Airborne measurements provide a means for accurate and fine-grained estimation of LST anisotropy (Cao et al., 2019). However, high cost involved in the experiments restricts these explorations to a few locations and a brief temporal window (Jiang et al., 2022). In comparison, the publicly available 70-m ECOSTRESS LST product with a large swath width provides sufficient spatial details at different times of day and night (Chang et al., 2021). Hence, the integration of ECOSTRESS's multi-angle LST measurements and parametric models holds great promise to examine the thermal anisotropy over urban areas.

Taking the City of Phoenix, Arizona, United States, as the study area, this paper employed ECOSTRESS LST observations acquired from May 2019 to March 2023 and two kernel-driven models to assess the urban thermal anisotropy and its diurnal and seasonal variations at the city scale and the local scale, i.e., across Local Climate Zones (LCZs). Specific objectives of this study are: 1) to develop a method for generating a quasi-simultaneous multi-angle ECOSTRESS LST dataset; 2) to characterize the city-scale and LCZ-scale LST anisotropy at different times of day in summer and winter; and 3) to validate the performance of different kernel-driven models by using clear-sky Landsat LST images. To our knowledge, this study is the first exploration of urban LST

anisotropy at 200-m fine spatial resolution based on satellite observations.

## 2. Study area and data

### 2.1. Study area

Phoenix, Arizona, is at the central hub of a vast metropolitan area situated in the northern periphery of the Sonoran Desert. With a population of approximately 1.6 million and covering an expansive territory of about 1340 km$^2$, it holds the distinction of being the fifth-largest city in the U.S.A. Our study focuses exclusively on the region within the municipal boundaries of the Phoenix City, centered at 33.4° N, 111.9° W (Fig. 1a). Nestled within a valley, Phoenix boasts an average elevation of 340 m and experiences predominantly gentle winds (Connors et al., 2012). Known as one of the hottest cities in the nation, it has a subtropical desert climate characterized by scorching, long, clear summers and mild winters. July stands out as the pinnacle of sweltering temperatures, with daily air temperature (AT) regularly surpassing 40 °C, while daily mean AT in winter hovers around an average of 13 °C. The annual precipitation remains relatively low, with an average of slightly over 200 mm. Phoenix has diverse land covers and uses, encompassing residential, commercial, industrial, grass, open soil and agriculture areas. As an initial exploration of the performance of ECOSTRESS LST observations in unraveling the fine-grained urban thermal anisotropy, this study selected Phoenix as the study area, primarily considering the availability of multi-angle ECOSTRESS sampling. In Phoenix, there are large ECOSTRESS LST samples over urban areas to generate diurnal and seasonal anisotropy profiles for different Local Climate Zones (LCZs) in comparison to other popular cities in thermal anisotropy research, such as Toulouse and Marseille (Fig. S1 and S2). Furthermore, such a selection holds the potential for continued in-depth investigation of urban thermal anisotropy as Phoenix has been a focal point for many other studies on LST and SUHI (Brandi et al., 2024; Logan et al., 2020). Fig. 1 provides detailed information on the specific geographic domain of the study area, the spatial distribution of meteorological stations, LCZ mapping, and the diurnal cycling patterns of summer and winter AT and LST at five selected meteorological stations. All times used in this study are local time (UTC - 7).

### 2.2. ECOSTRESS LST data

The multi-angle LST data are sourced from the ECOSTRESS level-2 product, namely ECO2LSTE, available for download on NASA's LPDAAC website (https://lpdaac.usgs.gov/). The LST data has a spatial resolution of 70 m and is acquired at various times throughout the day

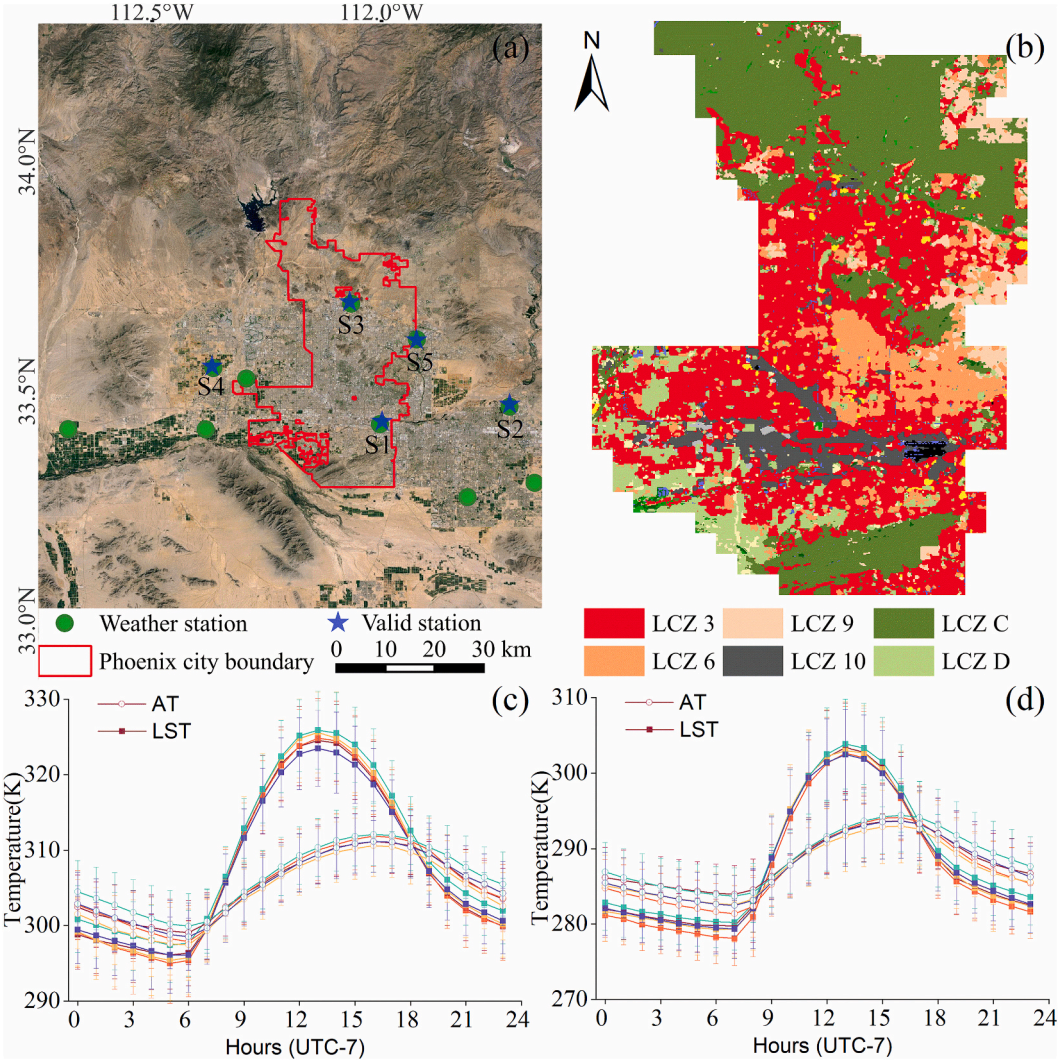


**Fig. 1.** The study area – Phoenix, Arizona, in the U.S.A. (a) The location of Phoenix City. (b) The LCZ classifications at 100 m spatial resolution. The seasonal mean air temperature (AT) and land surface temperature (LST) at the five meteorological stations in summer (c) and winter (d). S1-S5 denote the identification numbers of the meteorological stations utilized in this study.

on different dates (Hulley et al., 2021). ECO2LSTE product includes simultaneously retrieved spectral emissivity and LST, generated using the physical-based Temperature Emissivity Separation (TES) algorithm. The TES approach employs the RTTOV radiative transfer model, in conjunction with dynamic atmospheric profiles derived from the NASA Global Modeling and Assimilation Office GEOS5-FP reanalysis product, to accurately correct the observed radiances for atmospheric effects (Hook et al., 2020). The quality and accuracy of the ECOSTRESS LST data have been extensively validated by the ECOSTRESS science team and exhibited good consistency with ground LST records across diverse global validation sites ($r^2$ = 0.99, RMSE = 1.07, and MAE = 0.4 K) (Hulley et al., 2021). For this study, we gathered all available ECOSTRESS LST scenes spanning from May 2019 to March 2023 covering the Phoenix City region. These multi-angle data were further categorized into two groups: the summer group, comprising data from May to September, and the winter group, comprising data from November to March. April and October were regarded as the transition months between winter and summer. This study extended the duration of summer and winter in Phoenix based on its climatic characteristics, aiming to obtain more available ECOSTRESS samples. This partitioning can be supported by previous literature and official climate records (https://azclimate.asu.edu/climate/climate-of-phoenix-summary/). Analysis of monthly climate data spanning from 1991 to 2020 revealed that the mean temperature during May to September typically ranged from 25 °C to 35 °C, while the average temperature during November to March was generally in the 10 °C to 20 °C range (Fig. S3).

### 2.3. Ancillary data

This study employed data from ECOSTRESSS level-1 Geolocation (ECO1BGEO) and level-2 Cloud Mask (ECO2CLD) products to determine the solar/sensor azimuth and zenith angles corresponding to each ECOSTRESS LST pixel and to identify the presence of cloud coverage. These datasets were also obtained from NASA's LPDDAC.

Hourly LST data were derived from the Advanced Baseline Imager (ABI) sensor on board the new-generation geostationary satellite – GOES-16, which belongs to the GOES-R series of satellites and serves as the eastern satellite. The publicly available GOES-R LST product has a temporal resolution of 1 h and a spatial resolution of 2 km and has undergone evaluation using observations from other satellite platforms and in-situ stations (Yu and Yu, 2020). In this study, we obtained GOES-R LST for four years from May 2019 to March 2023 from the National Oceanic and Atmospheric Administration (NOAA, https://www.avl.class.noaa.gov/). These data were then combined with AT measurements to assist in generating the quasi-simultaneous multi-angle ECOSTRESS LST dataset.

Hourly AT data were obtained from the National Centers for Environmental Information in NOAA (https://www.ncei.noaa.gov/). We identified all meteorological stations within the study area and its surrounding region, as depicted in Fig. 1a. Ultimately, five stations consistently provided high-quality AT records at hourly intervals from May 2019 to March 2023. The data from these five selected stations was utilized for subsequent relevant analyses.

The LCZ map of Phoenix was downloaded from LCZ generator provided by the World Urban Dataset and Access Portal Tools (WUDAPT, https://www.wudapt.org/). The LCZ map corresponds to July 2020 and has a 100-m spatial resolution with an $OA_{bu}$ (overall accuracy of the built and natural LCZs) value of 0.96. Additionally, it is available in GeoTIFF format and consists of three layers: LCZ, LCZ-filter, and class probability (Demuzere et al., 2021). We used the LCZ-filter layer to characterize the spatial heterogeneity of the urban environment in the study area (Fig. 1b). In this study, we further employed tree canopy cover and elevation to refine and filter more representative LCZ classifications. We used tree canopy cover for the year 2021 by the U.S. Forest Service and elevation data product by NASA's Shuttle Radar Topography Mission (STRM) team, accessible for download at https://data.fs.usda.gov/ and https://earthexplorer.usgs.gov/. Both datasets have a spatial resolution of about 30 m.

Landsat LST data was acquired from the USGS Landsat 8–9 Collection-2 Surface Temperature product (https://earthexplorer.usgs.gov). Observed from the nadir, Landsat 8/9 thermal data has a temporal revisit interval of 16 days and a 100-m native spatial resolution. To ensure consistency, we selected clear-sky imagery with acquisition dates and diurnal time points similar to the ECOSTRESS scenes in summer, with a maximum difference of three days. Finally, three Landsat images (path/row: 37/37), acquired on June 3, June 11, and August 6, 2022, were collected in this study to validate the model performance.

## 3. Methodology

Figure 2 presents the procedure for exploring urban thermal anisotropy with multi-angle ECOSTRESS LST observations. The procedure entails four main steps: 1) generating a quasi-simultaneous multi-angle ECOSTRESS LST dataset, 2) mapping LCZ at a spatial resolution of 200 m, 3) Simulating city-scale and LCZ-scale LST anisotropic patterns at different times, and 4) performing validation. The specific details of the steps are described in the subsequent sections.

### 3.1. Generating a quasi-simultaneous multi-angle ECOSTRESS LST dataset

We developed a method to generate a quasi-simultaneous multi-angle ECOSTRESS LST dataset with the assistance of hourly AT and GOES-R LST. As previously mentioned, although the collected ECOSTRESS LST are multi-angle data, they are typically acquired at varying times of day and on different days, which renders them unsuitable for direct anisotropy assessment. Hu et al. (2016) proposed a method to obtain a quasi-simultaneous MODIS LST dataset by subtracting the effects of atmospheric and weather variations. This method opens an efficient avenue to evaluate satellite-derived LST angular effect at large spatial scales and over long time periods (i.e., multi-year seasonal average). Recently, Wang et al. (2022b) simplified this method by further determining the impact of atmospheric effect. Consequently, they modified the method to solely account for weather variability, enabling the acquisition of the quasi-simultaneous MODIS LST dataset. Based on that simplified method, the LST anisotropy of 25 global cities was evaluated at the city scale, where anisotropy was defined to merge the impact of angular emissivity and angular atmospheric attenuation. The ECOSTRESS LST product incorporates real-time atmospheric profiles to achieve accurate atmospheric correction, leading to less bias compared to the MODIS LST product and negligible influence on LST variations. Therefore, the focus of this study is to eliminate the impact of weather variations and diurnal cycling on diverse ECOSTRESS thermal scenes, so as to obtain an LST dataset that is only relevant to observational angles (Schematic is given in Fig. S4 in Appendix).

For all ECOSTRESS scenes captured between May 2019 and March 2023, we initially performed data preprocessing using the corresponding cloud mask and quality control files to acquire a cloud-free ECOSTRESS LST dataset. We then divided the cloud-free ECOSTRESS LST dataset into two parts (i.e., summer and winter) based on the acquisition dates of the data. During this process, imagery with less than 50 % valid pixel count in the study area was discarded. For each part, we further classified ECOSTRESS LST images with similar observation hours into groups. Specifically, we partitioned a diurnal cycle into 24 integer hours, ranging from 0 to 23, based on the acquisition times of the hourly GOES-R LST data. Then, the ECOSTRESS LST data obtained within a half-hour window before and after each hour were consolidated into the same group. Ultimately, we garnered 24 ECOSTRESS LST sets for both summer and winter, respectively. Afterward, these data were processed by the following steps to generate quasi-synchronized multi-angle LST observations for varying hours, with the assumption of stable weather conditions within an hour in the study area.

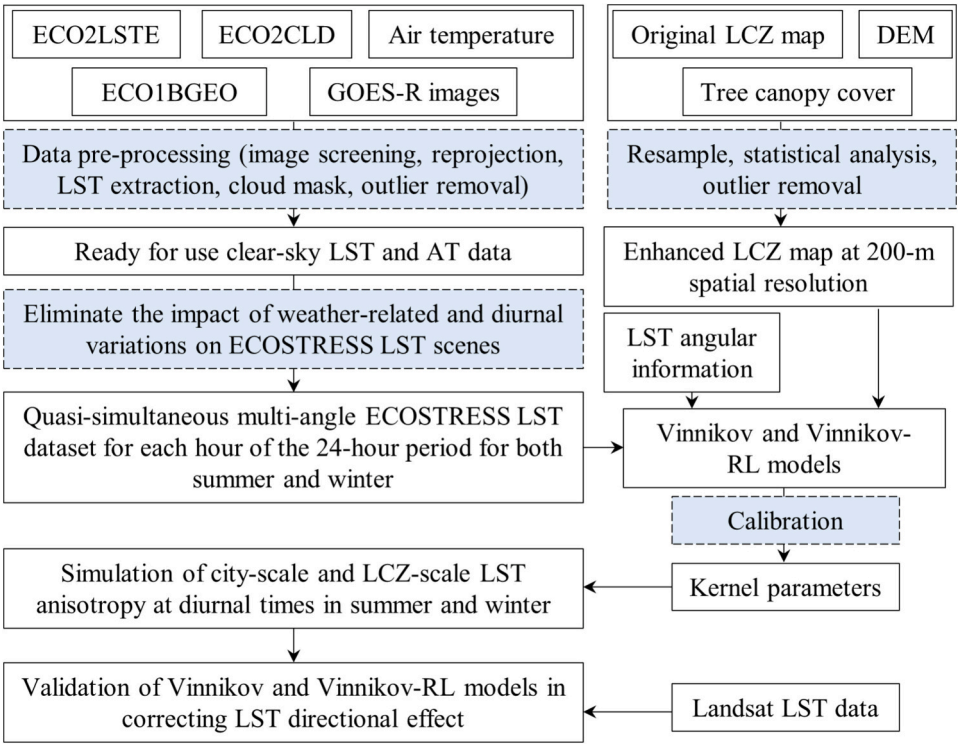


**Fig. 2.** Flowchart of the analytical procedures conducted in this study.

For each clear-sky ECOSTRESS LST scene (acquisition time $t_1$), we ascertained the hour $t$ of its corresponding group (where $t - 0.5 < t_1 \leq t + 0.5$). Then, we subtracted the weather-related signal, $LST_{wea}(t)$, and the bias caused by diurnal LST variation, $\Delta LST_{Diurnal}(t_1)$, from this image, as shown in Eq. 1.

$$ELST_{Quasi}(\mathrm{t}) = ELST(t_1) - \Delta LST_{Diurnal}(t_1) - LST_{wea}(\mathrm{t}) \quad (1)$$

where $ELST_{Quasi}(t)$ denotes a generated quasi-simultaneous multi-angle ECOSTRESS LST image for hour $t$, and $ELST(t_1)$ is the original clear-sky ECOSTRESS LST acquired at time $t_1$.

First, we calculated $LST_{wea}(t)$ using AT measurements obtained from meteorological stations and high temporal resolution LST observations derived from GOES-R, as detailed in Eqs. 2–8. Angle-independent AT was employed to determine the impacts of weather variability on AT and LST variations. Temporal variation of AT is commonly recognized as accounting for only a portion of the overall variation in LST. Thus, the coefficient $a$ was introduced to adjust the influence of weather-induced anomaly from AT on LST (Hu et al., 2016; Wang et al., 2022b).

$$T_{air}(x,y,t) = \overline{T_{air}(x,y,t)} + T_{air,wea}(x,y,t) \quad (2)$$

$$LST_{wea}(x,y,t) = a(\mathrm{x},\mathrm{y}) \times T_{air,wea}(x,y,t) \quad (3)$$

where $(x,y)$ denotes a given location of a GOES-R LST pixel or meteorological station, $T_{air}(x,y,t)$ and $\overline{T_{air}(\mathrm{x},\mathrm{y},t)}$ are the observed and seasonal average AT at hour $t$ (i.e., each hour in the 24-h diurnal cycle), respectively, $T_{air,wea}(x,y,t)$ and $LST_{wea}(x,y,t)$ signify the weather-related AT and LST variations, respectively, and $a(x,y)$ is the adjustment coefficient.

Then, the coefficient $a(x,y)$ for each station is determined by fitting long-term clear-sky GOES-R LST and AT records at different seasonal (i.e., summer and winter) and temporal (i.e., hour $t$ in the 24-h diurnal cycle) points using the Eq. 4. We calculated different $a$ values for the summer and winter diurnal cycles over 24 h, and the results are presented in Table S1 in Appendix.

$$LST(x,y,t) = a(\mathrm{x},\mathrm{y}) \times T_{air}(x,y,t) + \mathrm{b}(\mathrm{x},\mathrm{y}) \quad (4)$$

The subsequent task is to estimate the spatial distribution of the impact of weather variability on LST variations. Since the weather-related signal in this study represents temperature deviations from the seasonal average as described in Eq. 2, we decomposed the GOES-R LST using Eq. 5, where $\varepsilon(x,y,t)$ can be regarded as the random error of observation (Vinnikov et al., 2008).

$$GLST(\mathrm{x},\mathrm{y},t) = \overline{\mathrm{GLST}(\mathrm{x},\mathrm{y},t)} + LST_{wea}(\mathrm{x},\mathrm{y},\mathrm{t}) + \varepsilon(\mathrm{x},\mathrm{y},\mathrm{t}) \quad (5)$$

where $GLST(x,y,t)$ and $\overline{\mathrm{GLST}(\mathrm{x},\mathrm{y},t)}$ represent the observed and seasonal average GOES-R LST, respectively.

In the study area, there are five meteorological stations providing continuous, high-quality AT measurements at hourly intervals, as shown in Fig. 1. We can obtain the value of $\varepsilon(x,y,t)$ for each station location using Eq. 6. For the same satellite radiometer, the random error of observation is more dependent on time, varying with diurnal cycles or wet/dry atmospheric conditions, while the spatial dependence is weak and can be ignored for nearby pixels (Vinnikov et al., 2011). Thus, we assume a constant random error of observation for each individual GOES-R LST image over the study area. Subsequently, the $\varepsilon(t)$ term was introduced to adjust the individual GOES-R LST image and obtain the spatial distribution of the impact of weather variability on LST. In this study, $\varepsilon(t)$ was estimated as the average of $\varepsilon(x,y,t)$ obtained from the five meteorological stations across the study area, as shown in Eq. 7.

$$\begin{aligned}\varepsilon(\mathrm{x},\mathrm{y},\mathrm{t}) &= GLST(\mathrm{x},\mathrm{y},t) - \overline{\mathrm{GLST}(\mathrm{x},\mathrm{y},t)} - LST_{wea}(\mathrm{x},\mathrm{y},\mathrm{t}) \\ &= GLST(\mathrm{x},\mathrm{y},t) - \overline{\mathrm{GLST}(\mathrm{x},\mathrm{y},t)} - a(\mathrm{x},\mathrm{y}) \times (T_{air}(\mathrm{x},\mathrm{y},t) - \overline{T_{air}(\mathrm{x},\mathrm{y},t)})\end{aligned} \quad (6)$$

$$\varepsilon(\mathrm{t}) = \overline{\sum_{n=1}^{5} \varepsilon(\mathrm{x_n},\mathrm{y_n},\mathrm{t})} \quad (7)$$

Following that, the spatial distribution of the impact of weather variability on LST, denoted as $LST_{wea}(t)$, can be estimated using Eq. 8 when a clear-sky GOES-R LST sample ($GLST(t)$) is available at the corresponding time. To sum up, the impact of weather changes on LST

variations was determined by the angle-independent AT, and further estimation of their spatial distribution at 2 km resolution was accomplished with the assistance of fixed-angle hourly observations from GOES-R.

$$LST_{wea}(t) = GLST(t) - \overline{GLST(t)} - \varepsilon(t) \quad (8)$$

This method was further validated using AT measurements from the meteorological stations. Specifically, we utilized data from four of the five available meteorological stations as inputs to the method, while reserving the observations from the remaining station for independent validation. AT and LST measurements at 12:00 (local time) with strong incoming solar radiation in summer and winter during the study period were employed to assess the correlation between the observed $LST_{wea}(t)$ at the validation station and the estimated $LST_{wea}(t)$ derived from the proposed method, thereby demonstrating the performance of the proposed method. Furthermore, we also included the commonly used approach of simply defining the weather-related LST changes as $LST(t_1) - LST(t_2)$ (the disparity between observed and reference LSTs) for comparison. The validation results presented in Fig. 3 demonstrate that the proposed method could effectively estimate the spatial distribution of the impact of weather variability on LST variations.

The remaining task was to reduce bias arising from diurnal variation in LST. Eqs. 9 and 10 were employed for each LST group to estimate the uncertainty at the GOES-R pixel scale caused by diurnal LST variation.

$$\Delta LST_{Diurnal}(t_1) = (t_1\text{-}t) \times (\overline{GLST(t)}\text{-}\overline{GLST(t\text{-}1)}), \quad t_1 \le t \quad (9)$$

$$\Delta LST_{Diurnal}(t_1) = (t_1\text{-}t) \times (\overline{GLST(t+1)}\text{-}\overline{GLST(t)}), \quad t_1 > t \quad (10)$$

where $\Delta LST_{Diurnal}(x,y,t_1)$ denotes the bias from the diurnal LST variation.

Finally, we subtracted the corresponding weather-related signal, $LST_{wea}(t)$, and bias caused by diurnal LST variation, $\Delta LST_{Diurnal}(x,y,t_1)$, from each clear-sky ECOSTRESS image in different LST groups, thereby obtaining a quasi-simultaneous multi-angle ECOSTRESS LST dataset. In this methodology, the weather-related LST variations were quantified as deviations from the seasonal mean values. Therefore, the dataset obtained by adjusting the ECOSTRESS LST observations based on this approach can be regarded as quasi-simultaneous multi-angle LST representing the seasonal average. Subsequently, three adjusted ECOSTRESS images for both summer and winter were employed to directly examine the angular effects on regional LST. These images were acquired during comparable diurnal periods, exhibiting similar solar

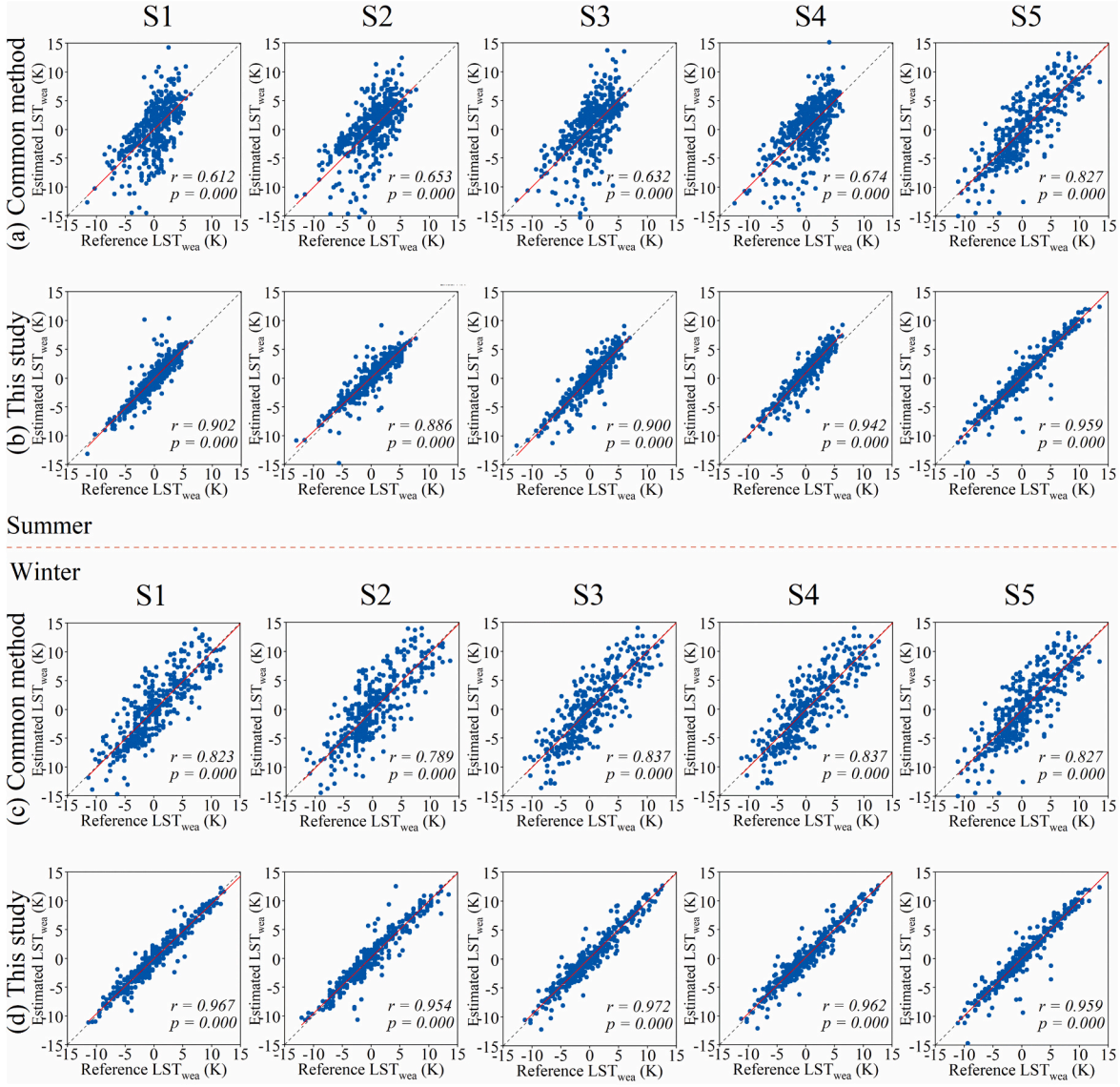


**Fig. 3.** Validation of the $LST_{wea}$ estimated by the proposed method vs. the commonly used method, against reference $LST_{wea}$ in summer (a, b) and winter (c, d). S1-S5 represent the meteorological stations used for independent validation (locations shown in Fig. 1).

zenith angle (SZA) and VZA differences, yet demonstrating notable disparities in solar azimuth angle (SAA) and VAA differences. We calculated the regional average and pixel-wise LST differences among these images.

### 3.2. Mapping local climate zones

This study partitioned Phoenix City into different LCZ classifications to gain new insight into the LCZ-scale LST anisotropy. LCZ scheme provides a standardized methodology for investigating the spatial heterogeneity of the urban thermal environment by associating specific climate-related physical parameters within predefined ranges to each LCZ (Huang et al., 2023). Generally, LCZ of the same type is presumed to exhibit similar thermal characteristics within a local context (Stewart and Oke, 2012). Given the spatial resolution of ECOSTRESS LST at around 68 m, we resampled the LCZ map to 200 m, creating a grid consisting of 3 × 3 LST pixels and 2 × 2 original LCZ pixels. Meanwhile, the 200 m grid would be designated with the corresponding LCZ type only if all 4 pixels within it belong to the same LCZ type. After that, LCZ delineation of the study area was refined by applying additional filters based on tree canopy cover and elevation-derived slope data. First, we computed the average tree canopy cover and slope, along with their corresponding standard deviations (SD), for each LCZ type. Second, we retained the LCZs within each LCZ type that satisfied the criterion of having tree canopy cover and slope values that fell within the range of mean ± SD. Ultimately, we generated the 200-m spatial resolution LCZ map for the study area, comprising LCZ 3, 6, 9, 10, C, and D with pixel counts of 11,934, 2463, 1325, 1483, 10,594, and 1601, respectively. The definitions and conceptual diagram of different LCZ classifications are presented in Table 1 and Fig. S5 (see Appendix). Using six ECOSTRESS images, the LCZ classifications were evaluated by comparing the mean LST and SD across different LCZs.

### 3.3. Simulating city-scale and LCZ-scale LST anisotropic patterns at different times

This study employed the Vinnikov model and Vinnikov-RL model to assess LST anisotropic patterns and their diurnal dynamics during summer and winter at both city and LCZ scales based on the generated quasi-simultaneous multi-angle ECOSTRESS LST dataset. The selection of the Vinnikov and Vinnikov-RL models was motivated by their high simulation accuracy and widespread usage in anisotropic research based on satellite LST data (Cao et al., 2021; Ran et al., 2022). Furthermore, they can respectively represent independent three-parameter kernel-driven models and coupled four-parameter kernel-driven models, enabling us to evaluate their individual performance when applied to ECOSTRESS LST data. The quasi-simultaneous multi-angle 70-m ECOSTRESS LST dataset that we generated comprised data for each hour of the 24-h period for both winter and summer.

**Table 1**
Detailed information of Local Climate Zone (LCZ) classifications in this study.

| LCZ class | Built type | Pixel count | Definition |
|---|---|---|---|
| LCZ 3 | Compact low-rise | 11,934 | Dense mix of low-rise buildings. |
| LCZ 6 | Open low-rise | 2463 | Open arrangement of low-rise buildings. |
| LCZ 9 | Sparsely built | 1325 | Sparse arrangement of small or medium-size buildings in a natural setting. |
| LCZ 10 | Heavy industry | 1483 | Low-rise and midrise industrial structures. Few or no trees. |
| LCZ C | Bush, scrub | 10,594 | Open arrangement of bushes, shrubs, and short, woody trees. |
| LCZ D | Low plants | 1601 | Featureless landscape of grass or herbaceous plants/crops. |

Reference: Stewart and Oke, 2012

The Vinnikov model was originally designed by Vinnikov et al. in 2012 to harmonize LST products derived from GOES series satellites. It was also used to facilitate the integration of LST datasets derived from SEVIRI and MODIS (Ermida et al., 2017). This model comprises three kernels in a linear combination: isotropic kernel, emissivity kernel, and solar kernel, which are mathematically expressed as follows:

$$\frac{T(\theta_s,\theta_v,\Delta\varphi)}{T_N} = 1 + A \times K_{Emissivity}(\theta_v) + \mathrm{D} \times \mathrm{K_{Solar}}(\theta_s,\theta_v,\Delta\varphi) \tag{11}$$

$$K_{Emissivity}(\theta_v) = 1 - cos\theta_v \tag{12}$$

$$\mathrm{K_{Solar}}(\theta_s,\theta_v,\Delta\varphi) = sin\theta_v cos\theta_s sin\theta_s cos(\theta_v - \theta_s) cos\Delta\varphi \tag{13}$$

where $A$, $D$, and $T_N$ (LST observed at nadir) are the three unknown parameters, $T(\theta_s,\theta_v,\Delta\varphi)$ denotes the LST observations, $\theta_s$ and $\theta_v$ represent SZA and VZA, respectively, and $\Delta\varphi$ is the difference between SAA and VAA.

Since $T_N$ at each diurnal hour was quite uncommon to be observed, Eq. 11 was then reformulated as Eq. 14 to better accommodate the features of the generated multi-angle ECOSTRESS LST dataset:

$$\frac{T_{E1}}{T_{E2}} = \frac{1 + A \times K_{Emissivity}(\mathrm{E1}) + \mathrm{D} \times \mathrm{K_{solar}}(\mathrm{E1})}{1 + A \times K_{Emissivity}(\mathrm{E2}) + \mathrm{D} \times \mathrm{K_{solar}}(\mathrm{E2})} \tag{14}$$

where *E1* and *E2* refer to quasi-simultaneous multi-angle ECOSTRESS LST observations in the same group (e.g., hour t), sharing the same $T_N$.

The Vinnikov-RL model, introduced by Ermida et al. (2018), is a combination of the Vinnikov model and the RL model (i.e., a nonlinear model with three unknown parameters focused on simulating the hotspot effect) (Duffour et al., 2016). In this model, the solar kernel in the Vinnikov model is replaced by the hotspot kernel from the RL model. The expression is provided below:

$$T(\theta_s,\theta_v,\Delta\varphi) = T_N + (A \times T_N) \times K_{Emissivity}(\theta_v) + \Delta T_{HS} \times \mathrm{K_{RL}}(\theta_s,\theta_v,\Delta\varphi,k) \tag{15}$$

$$K_{Emissivity}(\theta_v) = 1 - cos\theta_v \tag{16}$$

$$\mathrm{K_{RL}}(\theta_s,\theta_v,\Delta\varphi,k) = \frac{e^{-kf} - e^{-kf_N}}{1 - e^{-kf_N}} \tag{17}$$

$$f = \sqrt{tan^2\theta_s + tan^2\theta_v - 2tan\theta_s tan\theta_v cos\Delta\varphi} \tag{18}$$

$$\mathrm{f}_N = tan\theta_s \tag{19}$$

where $T_N$, $A$, $\Delta T_{HS}$, and $k$ are the four unknown parameters to be estimated. $\Delta T_{HS}$ denotes the temperature difference observed at the hotspot ($T_{HS}$), where the sun is situated near the sensor, and the nadir ($T_N$), $k$ is a scaling factor used to describe the hotspot width.

In this study, we introduced a new parameter $R$ defined as $(T_{HS} - T_N)/T_N$ to facilitate comparison of the results obtained from Vinnikov and Vinnikov-RL models. Physically, it quantifies the relative temperature variation between the hotspot and the nadir in relation to the nadir temperature and varies with changes in solar geometry. Then, Eq. 20 can be derived.

$$\frac{T(\theta_s,\theta_v,\Delta\varphi)}{T_N} = 1 + A \times K_{Emissivity}(\theta_v) + R \times \mathrm{K_{RL}}(\theta_s,\theta_v,\Delta\varphi,k) \tag{20}$$

Likewise, Eq. 20 is rewritten as Eq. 21 to align with the generated ECOSTRESS LST dataset.

$$\frac{T_{E1}}{T_{E2}} = \frac{1 + A \times K_{Emissivity}(\mathrm{E1}) + R \times \mathrm{K_{RL}}(\mathrm{E1,k})}{1 + A \times K_{Emissivity}(\mathrm{E2}) + R \times \mathrm{K_{RL}}(\mathrm{E2,k})} \tag{21}$$

According to the mathematical formulations of the two models (i.e., Eqs. 11 and 20), LST anisotropy was defined as $T(\theta_s,\theta_v,\Delta\varphi)/T_N$ in this study. We presented the angular distribution patterns of the quasi-simultaneous EOSTRESS LST dataset over the course of the diurnal

cycle for both summer and winter. Surface targets were used as references to define the azimuth and zenith angles, with valid ranges of [0°, 360°] and [0°, 90°], respectively. Then, urban mean and SD of VZA, VAA, SZA, and SAA for each LST imagery were calculated. Following that, we employed urban mean multi-angle LST to solve the Vinnikov model and simulated the anisotropy characteristics at the city scale. To mitigate the influence of clouds, only LST images with an effective pixel count exceeding 70 % along with their corresponding angles were selected as inputs. Under the assumption that both $A$ and $D$ values remained non-temporally dynamic, $A$ is initially computed based on nighttime observations, followed by the calibration of $D$ using daytime observations (Ermida et al., 2017; Vinnikov et al., 2012). The specific procedure was as follows: (1) For nighttime observations in summer and winter, data from local time 22:00 to 04:00 and 21:00 to 05:00, respectively, were utilized to minimize the influence of residual solar radiation. Daytime observations were conducted from 07:00 to 18:00 and 08:00 to 17:00, respectively. (2) Pairwise data (referred to as E1 and E2) were fed into Eq. 15, and the $A$ value was derived through linear regression based on all nighttime data. Notably, E1 and E2 must belong to the same hour group as defined before, ensuring that they share the same $T_N$ value. (3) After determining the value of $A$, parameter $D$ was calculated using a similar approach based on all daytime observations. Subsequently, based on the calibrated Vinnikov model, we performed angular correction on the seasonal mean GOES-R LST to obtain diurnal cycles of summer and winter $T_N$ in the study area. Finally, diurnal variations of maximum thermal difference resulting from LST anisotropy at the city scale ($Max_{diff}$) were computed as $T_N \times (\mathrm{Max}(T(\theta_s,\theta_v,\Delta\varphi)/T_N) - 1)$.

Benefiting from the high-resolution ECOSTRESS observations, this study further investigated the diurnal variations of thermal anisotropy signals in various LCZs during both summer and winter using the Vinnikov and Vinnikov-RL modeling approaches. To match the spatial resolution of LCZs, we first resampled each group of ECOSTRESS LST and its corresponding VAA, VZA, SAA, and SZA from approximately 70 m to 200 m. Subsequently, for the Vinnikov model, we calculated the values of parameters $A$ and $D$ for each LCZ pixel using Eq. 14 and the aforementioned procedure. Following the calibration, we computed seasonal averages and medians of $A$ and $D$ values for each LCZ category, which were then employed to simulate thermal anisotropy in different LCZs under a specific solar geometry. Furthermore, the instances of 12:00 during summer and winter, with solar geometry of (SZA: 17°, SAA: 151°) and (SZA: 50°, SAA: 171°), respectively, were employed to exemplify the impacts of sensor viewing angles on LST observations. For the Vinnikov-RL model, we obtained the $A$ value of each LCZ pixel using Eq. 21 based on the same procedure because the hotspot kernel was also assumed to be null at nighttime. Unlike parameter $D$, it is expected that both $R$ and $k$ would vary at different times during the day. Hence, we performed independent fitting of the parameters R and k for each LCZ pixel by employing separate groups of quasi-simultaneous multi-angle ECOSTRESS LST data, yielding corresponding parameter values for different hours within the diurnal cycle in different seasons. To address the issue of potential parameter instability during the fitting of the hotspot kernel, we have imposed constraints on the fitted parameter values based on the physical significance of $R$. The valid range of $R$ values was set to [0.00285, 0.178571]. Ultimately, five summer hours and three winter hours, which had a large proportion of valid fitted parameters (i.e., pairs of $R$ and $k$), were utilized to exhibit the diurnal variation of LST anisotropy at the LCZ scale.

### 3.4. Validation

This study validated the simulation results from the two models using clear-sky Landsat images. We extracted the average LST values of different LCZs from three pairs of ECOSTRESS and Landsat scenes acquired on adjacent dates and at similar diurnal times. Then, LST values for each LCZ obtained from ECOSTRESS imagery were adjusted to the nadir observation direction using the calibrated Vinnikov model and Vinnikov-RL model, respectively. To ensure comparability of the results among images, we substituted the absolute LST with the surface urban heat island (SUHI) of each LCZ, which was calculated as the difference between its LST value and the mean LST value of the LCZ D acquired in the same imagery. After that, we computed the Pearson correlation coefficients between Landsat-derived SUHI values and uncalibrated and calibrated ECOSTRESS SUHI values for different LCZs. In general, results obtained from the same observation direction demonstrate a stronger correlation, indicating higher comparability.

## 4. Results

### 4.1. Quasi-simultaneous multi-angle ECOSTRESS LST and enhanced LCZ map for thermal anisotropy assessment

With the assistance of GOES-R LST and in-situ AT data, we generated 24 sets of multi-angle ECOSTRESS LST data for both summer and winter, with one set per hour within the 24-h diurnal cycle. This dataset provides useful information on the LST anisotropy induced by differences in sun-surface-sensor geometries, particularly the variation of LST anisotropy with respect to the sensor viewing azimuth angle (Fig. 4). Fig. 4a, b and c show the spatial distribution of LST in the study area at 12:00 during the summer, with variations in observation angles. E1, E2, and E3 had similar differences in SZA and VZA (i.e., $D_{ZA}$) while exhibiting distinct patterns of SAA and VAA (i.e., $D_{AA}$). Obvious thermal disparities were observed among them, with E1 and E2 displaying a noticeably larger high-temperature area than E3. E1 and E2 possessed closely comparable average regional LST of 328.8 K and 328.1 K, respectively, which were significantly higher than E3's LST of 325.9 K observed from the opposite direction. The pixel-level analysis in Fig. 4d provided more detailed evidence for these anisotropy-caused LST differences. Fig. 3e, f and g illustrate the variations in LST at 11:00 during the winter under varying observation angles. E4, E5, and E6 had average LST of 297.5 K, 296.7 K, and 296.3 K, respectively, implying a temperature decrease with increasing deviation of the satellite VAA from the SAA. Similarly, more hotspots were observed when the sensor was positioned on the same side as the sun. Additionally, LST variations observed among these images indicated partial evidence of seasonal fluctuations in thermal anisotropy characteristics (Fig. 4d and h).

We partitioned the study area into different LCZs with a spatial resolution of 200 m while applying slope and tree canopy cover as filters to enhance their representativeness (Fig. 5a). It can be seen that dominant LCZ classifications in the study area were LCZ 3 and C, distributed in the central and northern portions of the region, respectively. Meanwhile, we examined the LCZ map with multiple thermal images (i.e., E1, E2, E3, E4, E5, and E6 in Fig. 4). As expected, LCZs exhibited different thermal patterns, and these discrepancies were consistently portrayed across varying images (Fig. 5b and c). For example, during midday in summer, LCZ C generally tended to have the highest LST, whereas LCZ D displayed the lowest values, with an average LST difference of about 4 K (Fig. 5b). Furthermore, there are smaller LST variations within the same LCZ, as evidenced by LST standard deviations predominantly ranging from 1 K to 2 K in summer and ranging from 0 K to 1 K in winter.

### 4.2. City-scale and LCZ-scale LST anisotropy simulated by the Vinnikov model

Figure 6 illustrates the angular distribution of the quasi-simultaneous multi-angle ECOSTRESS LST dataset. In total, there were 164 samples during the summer, comprising 84 daytime samples and 80 nighttime samples, while the winter season yielded a relatively smaller sample size of 132, with 64 images taken during the daytime and 68 during the nighttime. In summer, the hours of 00:00, 12:00, and 23:00 exhibited the highest frequency of multi-angle observations, each accumulating 10 samples. Conversely, the time slots of 02:00 and 03:00 had the lowest occurrence, with only 3 samples each. In winter, the

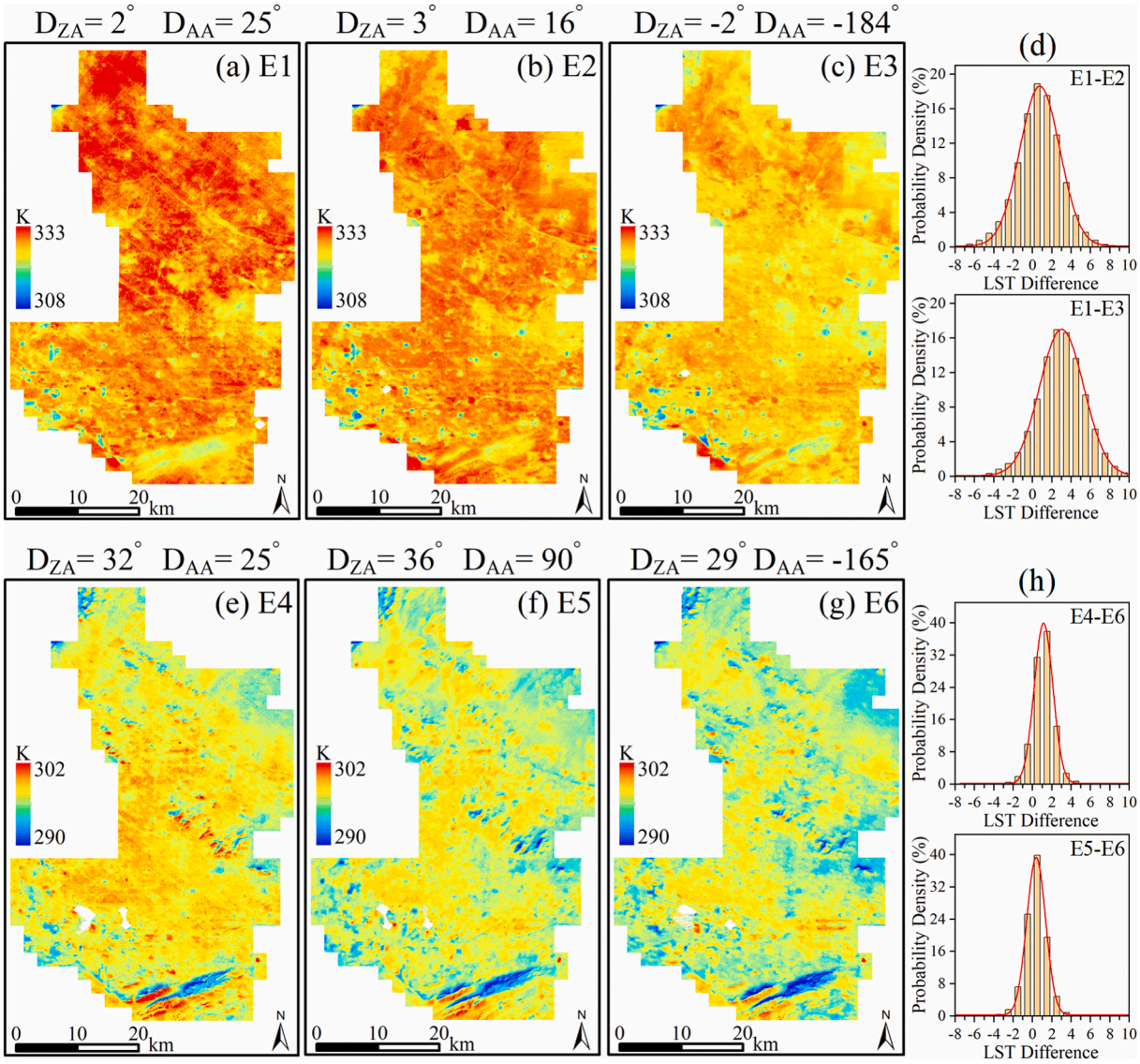


**Fig. 4.** Spatial distribution of the generated quasi-simultaneous multi-angle ECOSTRESS LST in the study area. The original ECOSTRESS imagery was obtained at: (a) E1: 11:32, 05 August 2022; (b) E2: 11:55, 06 August 2020; (c) E3: 11:32, 08 June 2020; (e) E4: 11:06, 08 February 2020; (f) E5: 10:39, 29 February 2020; (g) E6: 11:27, 06 February 2021. All times are local time (UTC-7). The pixel-wise LST difference among these images in summer (d) and winter (h). $D_{ZA}$ refers to the difference in zenith angles between the sun and the sensor. $D_{AA}$ denotes the difference in azimuth angles between the sun and the sensor.

hours of 16:00 and 18:00 recorded the highest number of samples, with 9 samples each. The time slot of 08:00 had the fewest samples, with only 2. The VZA was constrained within a narrow range of 30°, whereas the VAA spanned a wide range from 0° to 360°. This differed obviously from the angular patterns of the commonly used MODIS products, which featured VZA ranging from 0° to 65° and fixed VAA in two directions. Meanwhile, LST observations acquired on different dates corresponded to unique solar geometries. The SZA displayed significant variations, ranging from 0° to 90°, primarily influenced by the observation dates and time of day, while the SAA generally underwent regular changes from sunrise to sunset.

Figure 7 depicts the seasonal and diurnal variations of LST anisotropy at the city scale simulated by the Vinnikov model. In this study, the simulated hemispherical anisotropy features were constrained within a 30-degree VZA range, taking into account the sampling characteristics of ECOSTRESS. Meanwhile, the full 90-degree zenith angle range results at the city scale are presented in Fig. S6 in Appendix. The unknown parameters *A* and *D*, which depend on surface cover structure, were determined by fitting the model to the multi-angle urban mean LST data. In summer, the fitted value for *A* was 0.001 and for *D* was 0.036, whereas during winter, the value for *A* was 0.018 and for *D* was 0.038. Fig. 7a, b, c and d illustrate the spatial distribution of anisotropy at varying times of day in summer. During the daytime, the anisotropy exhibited a prominent hot spot effect, characterized by higher values when the sensor was located close to the sun and lower values when it was positioned opposite to the sun. For example, at 12:00 with SZA of 17° and SAA of 151°, the maximum thermal anisotropy ($T/T_N$) could reach 1.007, while the minimum was 0.994. Furthermore, different time periods within the diurnal cycle had distinct anisotropic patterns, manifested as varying ranges and intensities of hot and cold spots. At nighttime, as solar radiation diminished, the distribution of anisotropy became more uniform and its values decreased. Fig. 7f, g, h and i demonstrate the spatial distribution of winter anisotropy, which differed from that in summer. Furthermore, we obtained the maximum LST differences ($Max_{diff}$) induced by angular effects throughout the diurnal cycle, as shown in Fig. 7e and j. The $Max_{diff}$ demonstrated clear diurnal and seasonal variations. In summer, it exhibited an increase after sunrise, followed by a decrease at noon, another increase in the afternoon,

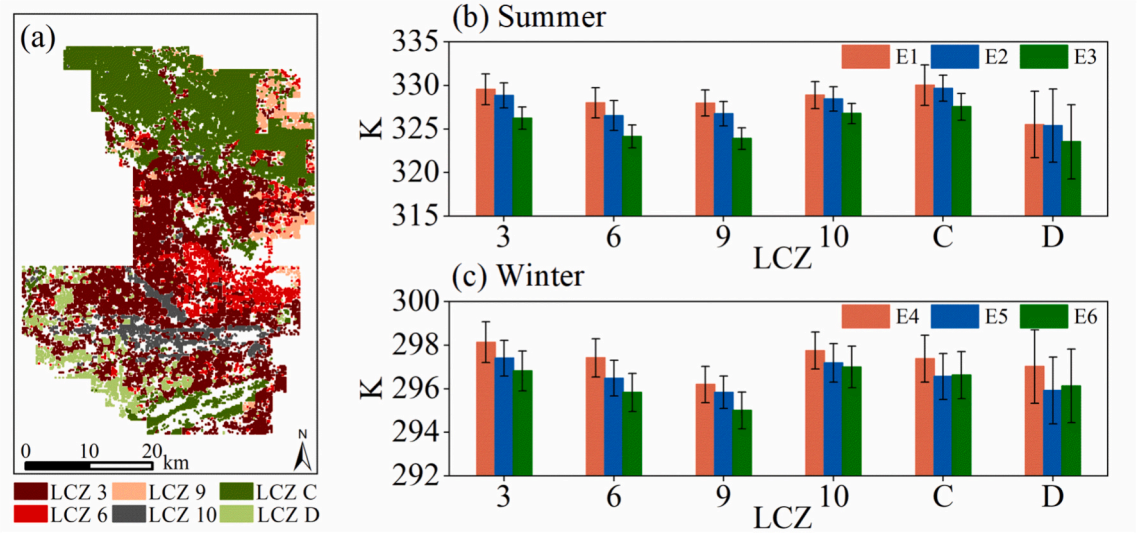


**Fig. 5.** LCZ delineation (a) and the thermal discrepancy in these LCZs (b and c).

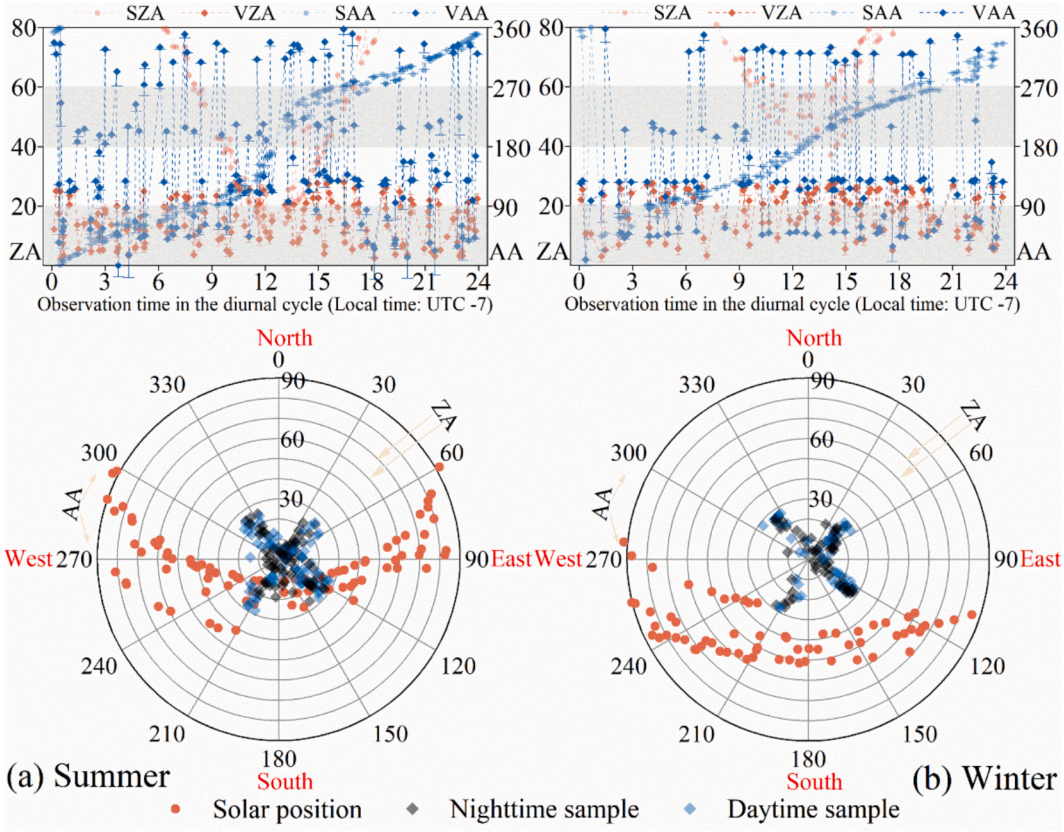


**Fig. 6.** Angular features of clear-sky ECOSTRESS LST data in Phoenix, Arizona, in summer (a) and winter (b). Time span: summer, May through September during 2019 to 2022; winter, November to March during 2019 to 2023.

and a relatively constant low value during the nighttime. In winter, it increased after sunrise, reached its peak and remained stable around midday, reduced in the afternoon, and remained constant at night. Moreover, the $Max_{diff}$ was generally higher in winter than in summer, with maximum value reaching approximately 10 K in winter and 5 K in summer.

Figure 8 presents the statistics of the calibrated values of parameters *A* and *D* for different LCZs based on the results from 9546, 1969, 1059, 1185, 8474, and 1281 LCZ pixels, respectively. We performed model parameter fitting for all LCZ pixels and then constructed boxplots for each LCZ using the values within the 10th and 90th percentiles to reduce noise. It can be found that these LCZs demonstrated similar variations in *A* values between different seasons. In summer, the mean *A* values for LCZ 3, 6, 9, 10, C, and D were − 0.001, 0.004, 0.005, −0.008, −0.001, and 0.021, while in winter, these values were 0.002, 0.004, 0.005, −0.006, 0.004, and 0.004, respectively. Compared to *A* values, the seasonal variation of parameter *D* values, which reflected the solar geometric effects, was more pronounced, with higher values in winter

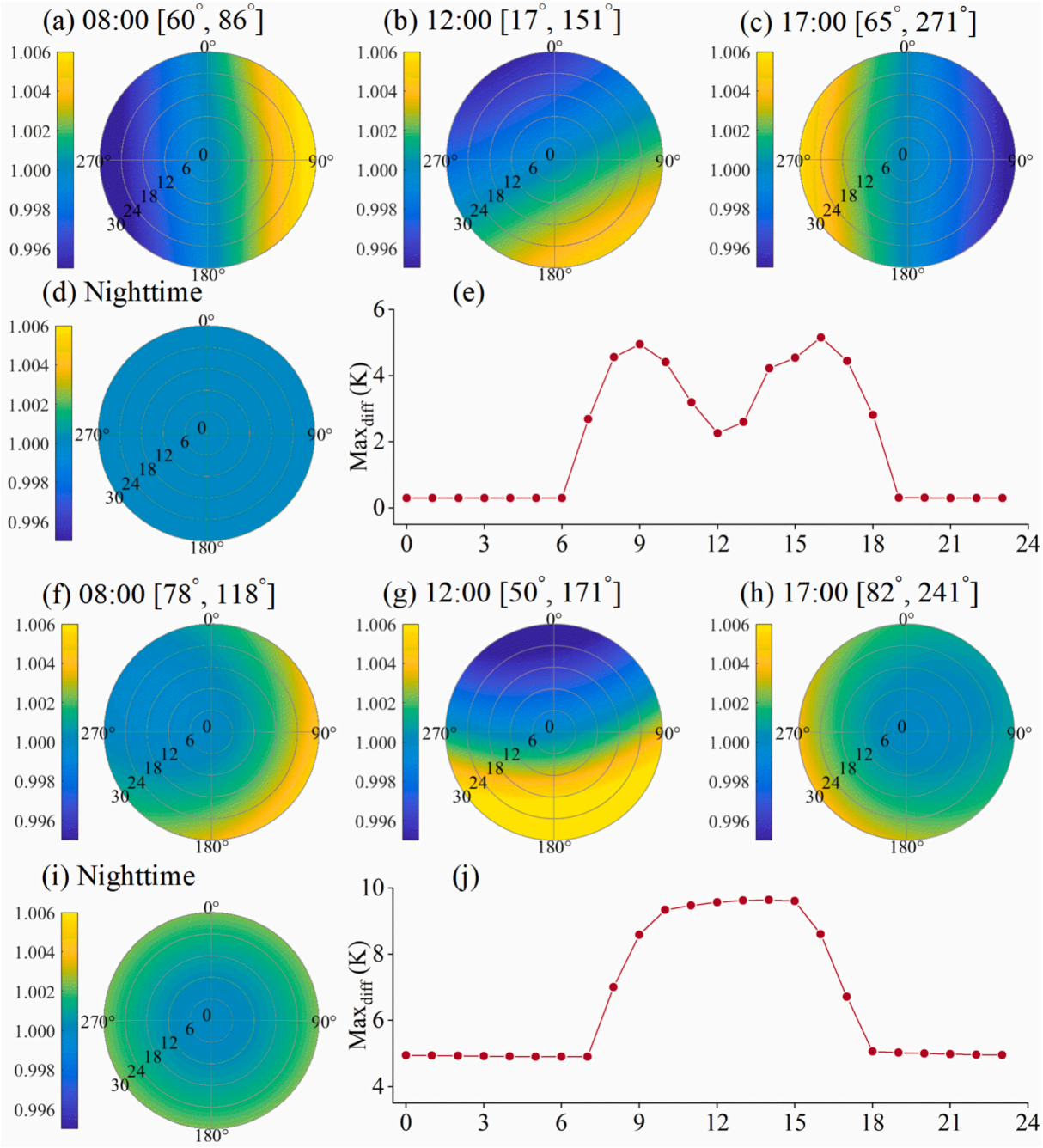


**Fig. 7.** The simulated city-scale LST anisotropic patterns at different times of day in summer (a, b, c, and d) and winter (f, g, h, and i) based on the Vinnikov model. The diurnal variations of the maximum LST differences that can be caused by angular disparities in summer (e) and winter (j).

across different LCZs. This could be partially explained by the obvious increase in LST contrasts among different facets due to the heating effect of solar radiation in colder environmental conditions during winter, resulting in greater anisotropy. This finding was consistent with that at the city scale. Additionally, the discrepancy in $D$ values among LCZs was also notable, with summer averages of 0.032, 0.037, 0.036, 0.031, 0.027, and 0.029, and winter averages of 0.048, 0.038, 0.037, 0.048, 0.035, and 0.048, respectively.

Figure 9 shows the spatial distribution of LST anisotropy ($T/T_N$) across LCZs simulated by the Vinnikov model. The simulations were conducted at 12:00 in both summer and winter, with solar geometry of (SZA: 17°, SAA: 151°) and (SZA: 50°, SAA: 171°), respectively. In summer, LCZ 6, 9, and D demonstrated more pronounced and larger hotspots. In winter, LCZ 3, 10, and D displayed larger hotspots, and their cold spot areas were also larger than other LCZs. The anisotropy magnitude of LCZs was notably higher in winter than in summer. Moreover, we quantified the maximum and minimum values of simulated anisotropy for each LCZ to provide a more direct understanding of the angular effects. In summer, the anisotropic values for LCZ 3 to D were as follows: (1.004, 0.996), (1.006, 0.996), (1.006, 0.996), (1.003, 0.995), (1.004, 0.996), and (1.007, 0.999), while in winter, they were (1.011, 0.990), (1.009, 0.992), (1.009, 0.992), (1.010, 0.988), (1.009, 0.992), and (1.012, 0.990), respectively.

### *4.3. Diurnality of LST anisotropic patterns in different LCZs by the Vinnikov-RL model*

We furthered our understanding of the directional anisotropy signals

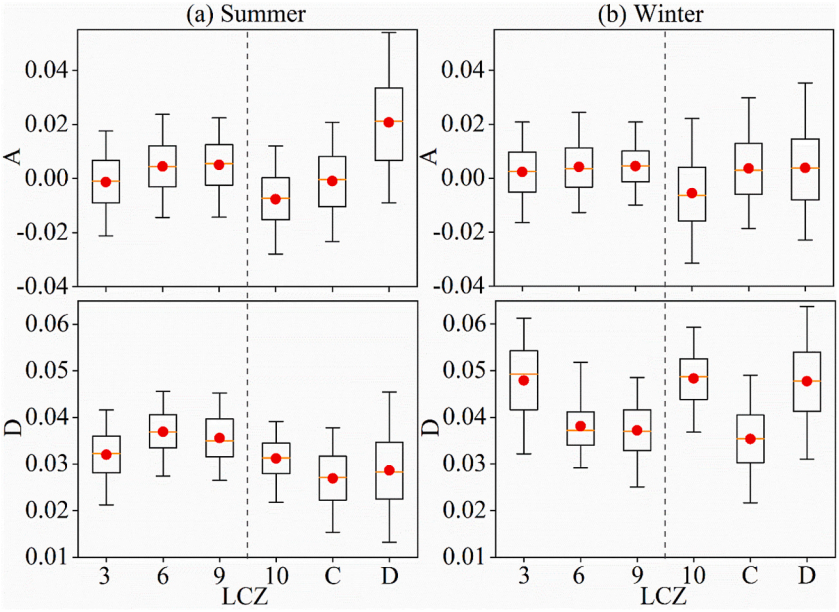


**Fig. 8.** Boxplots of the Parameter *A* and *D* for different LCZs in summer (a) and winter (b).

exhibited by different LCZs through the diurnal cycle using the Vinnikov-RL model. Due to the limited availability of multi-angle ECOSTRESS data, we could only obtain LCZ-scale LST anisotropy for a few specific hours during the day. The value of parameter *A* in the model for each LCZ was determined by nighttime observations, and its numerical value aligned with that of the Vinnikov model, as both models assume the absence of the solar kernel or hotspot kernel during daylight hours. Fig. 10 shows the statistical analysis of the remaining two parameters, *R* and *k*, in the Vinnikov-RL model, calibrated at 07:00, 10:00, 12:00, 14:00, and 15:00 during summer daytime. Specifically, *R* (i.e., $(T_{HS}\text{-}T_N)/T_N$) controls the intensity of the hotspot effect, while *k* adjusts the shape of the hotspot. A larger *R* value generally indicates a greater temperature difference between the solar incidence angle and the nadir angle, representing a stronger magnitude of LST anisotropy. Meanwhile, a larger *k* value signifies a narrower width of the hotspot. The *R* values of different LCZs demonstrated an overall higher trend around midday (i.e., 10:00 and 12:00) while displaying lower values in the morning and afternoon. In general, higher solar radiation was more likely to contribute to a stronger hotspot effect. Meanwhile, the *k* values manifested a similar pattern, with larger values at noon and smaller values in the morning and afternoon. To minimize the influence of outliers, we subsequently employed the median values of the *R* and *k* parameters to establish the model for simulating LST anisotropy for each LCZ.

The simulation results of diurnal variations in the LST anisotropy for different LCZs in the study area are depicted in Fig. 11 and Fig. S7 in the Appendix. It was evident that the Vinnikov-RL model outperformed the Vinnikov model in capturing the hotspot effect. The thermal anisotropy of LCZs exhibited distinct diurnal dynamics, with the hotspot effect being more pronounced and concentrated at noon. At varying times of day, LCZ 6, 9, and D usually displayed higher hotspot intensity and width than other LCZs. Furthermore, the thermal anisotropy signal of LCZ D, characterized by a landscape dominated by low plants, differed significantly from other built structures. The increased presence of trees in urban landscapes may alter the configuration of shadows in diverse directions, thereby contributing to a more complex anisotropy. We also summarized the maximum and minimum values of the LST anisotropy for LCZs at different times in the day and night, as presented in Table S2 in the Appendix.

Figure 12 demonstrates the statistics of the parameters *R* and *k* for different LCZs in winter, calibrated at 10:00, 13:00, and 14:00. The higher *R* values occurred at 14:00, followed by 13:00 and 10:00, indicating a stronger amplitude of hotspot effect at 14:00. The simulation results for each LCZ were shown in Fig. 13 and Fig. S8 in the Appendix. Overall, in winter, the cold spot effect was relatively more pronounced at various daytime moments. The hotspot effect was not significant at 10:00 but became prominent at 14:00. Moreover, LST anisotropy during the nighttime could be considered negligible. In comparison to 14:00 in summer, the hotspot domain and intensity were more notable at 14:00 in winter, but this contrast was reversed at 10:00. The seasonal variations in solar radiation intensity and direction, influenced by the position of the sun relative to the earth, led to disparities in heating efficiency among various landscape configurations, thereby making the attribution of LST anisotropy patterns in different LCZs more complex across seasons. Table S3 in the Appendix provided the maximum and minimum values of the simulated LST anisotropy for LCZs in winter.

### 4.4. Validation

The correlation of Landsat-derived SUHI with ECOSTRESS-derived SUHI, the Vinnikov-calibrated ECOSTRESS SUHI, and the Vinnikov-RL calibrated ECOSTRESS SUHI yielded 0.588 ($p < 0.05$), 0.669 ($p < 0.01$), and 0.851 ($p < 0.01$), respectively, as shown in Fig. 14. It was evident that obvious disparities existed between the ECOSTRESS observations acquired from different off-nadir angles and the Landsat observations at the nadir, although some discrepancies could be attributed to factors such as weather variations and systematic errors. The weak correlation implied limited comparability between them, which hindered the synergistic use of the two high-resolution remote sensing products. In contrast, the calibrated ECOSTRESS observations exhibited a strong correlation with the Landsat observations, highlighting the necessity and effectiveness of LST anisotropy correction. Furthermore, the results showed that the Vinnikov-RL model had better performance in quantifying the LST anisotropy than the Vinnikov model.

## 5. Discussion

Record-breaking high temperatures have led to increasingly severe health crises and economic losses, particularly in urban areas with dense populations. Fine-scale three-dimensional surface temperature modeling in cities is essential for significantly improving urban heat exposure and health assessments, and analyses of building energy

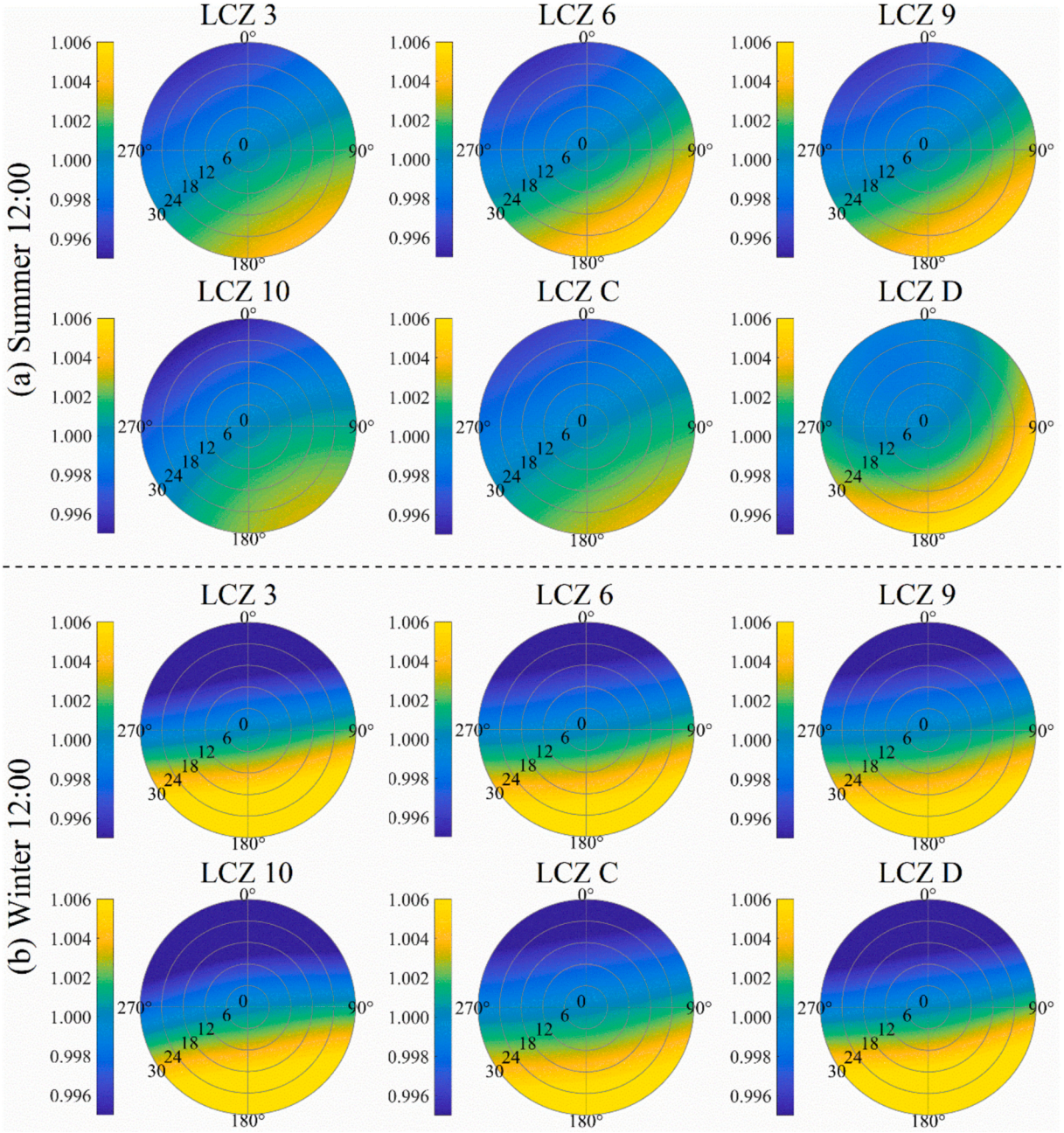


**Fig. 9.** The simulated LST anisotropic patterns of different LCZs at 12:00 in summer (a) and winter (b) based on the Vinnikov model.

consumption and heat emissions (Stewart et al., 2021). With the advancements in Space-Air-Ground integrated monitoring technologies, a pressing challenge in urban thermal remote sensing is the utilization of diverse LST datasets, particularly low-cost and spatially and temporally continuous satellite-derived observations, to estimate detailed three-dimensional surface temperatures (Li et al., 2023). This study is the initial step in addressing this challenge by analyzing LST anisotropy using high spatial and temporal resolution ECOSTRESS observations, establishing a foundation for the forthcoming synergistic utilization of aerial and satellite data. LST anisotropy research also holds great significance for enhancing the quality of remote sensing data products, a deeper understanding of spatiotemporal variations in surface energy fluxes, land surface process and climate models. This study investigated the characteristics of urban thermal anisotropy and its diurnal/seasonal variations for different LCZs with multi-angle ECOSTRESS LST data from space. To our knowledge, it is the first exploration of urban LST directional effects at 200-m fine spatial resolution based on space-borne observations. The results can contribute to understanding and application of satellite-derived multi-angle thermal data in complex urban environments and also have implications for improving the spatiotemporal comparability of multi-source LST products and achieving their harmonization.

### 5.1. *Benefits of ECOSTRESS observations in exploring directional variability of urban LST*

This research offers a valuable reference for characterizing the urban thermal anisotropy at fine spatial and temporal scales using ECOSTRESS LST product. The diverse building morphology and arrangements complicated the directional thermal anisotropy in the urban domain, necessitating more relevant efforts to optimize urban remote sensing measurement (Hu and Wendel, 2019). This study showcases and

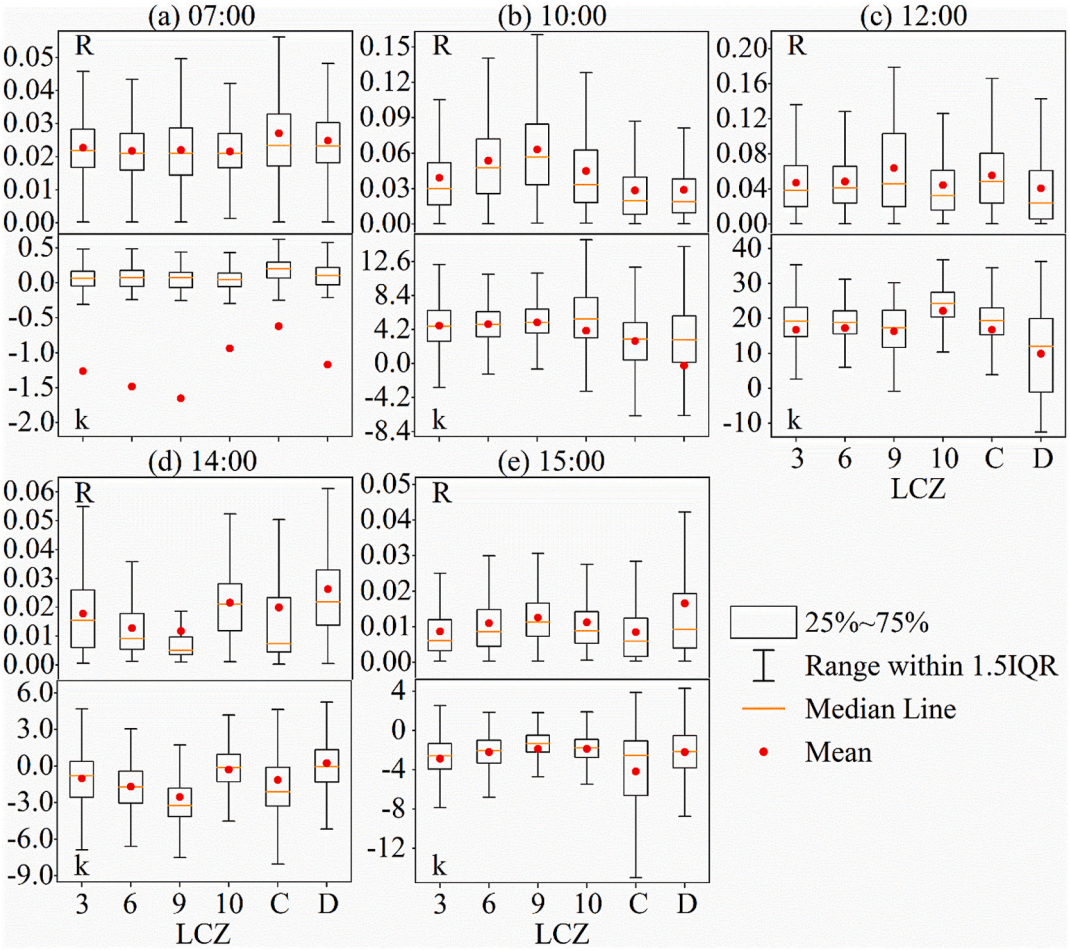


**Fig. 10.** Boxplots of the Parameter *R* and *k* for different LCZs at varying times over the 24-h diurnal cycle in summer: (a) 07:00, (b) 10:00, (c) 12:00, (d) 14:00, and (e) 15:00.

highlights the potential of new ECOSTRESS observations in exploring the directional variability of urban LST. The results demonstrated that ECOSTRESS, with its high-frequency and finer-resolution measurements, enables a more detailed characterization of the heterogeneity in urban LST anisotropy at large spatial scales. Compared to prevailing studies on anisotropy based on 1 km or coarser satellite observations, the introduction of multi-angle ECOSTRESS LST dataset is capable of capturing a wider range of urban surface types, thereby benefiting the assessment and development of practical parametric models that can be implemented at various satellite scales (Qin et al., 2023; Wang et al., 2023). In recent years, unmanned aerial vehicle (UAV) observations have been increasingly utilized for studies on thermal anisotropy over different underlying surfaces. However, UAV-based experiments are constrained to small-scale investigations at sub-meter resolutions (Bian et al., 2021; Jiang et al., 2022). ECOSTRESS observations can server as a valuable complement to current anisotropic studies, as with 70 m spatial resolution it can bridge the gap between existing satellite and UAV measurements (Cao et al., 2019; Yang et al., 2020). Furthermore, the integration of ECOSTRESS data with UAV-based experiments holds promise for separating land surface component temperatures to enhance urban climate research.

Accordingly, we proposed an effective approach for generating a quasi-simultaneous multi-angle ECOSTRESS LST dataset by eliminating the impacts of weather-related and diurnal LST variations. In this method, angle-independent air temperature was used to estimate the impacts of weather variability on the variations in AT and LST, which is a widely employed approach in current studies (Hu et al., 2016; Wang et al., 2022b). To meet the objective of this study, we refined the methodology by utilizing hourly GOES-R LST observations to distribute weather-related temperature anomalies, as captured by in-situ air temperature, onto 2-km grids over the study area. Specifically, an adjustment term $\varepsilon(t)$ was introduced to account for the random error of GOES-R observation and to mitigate the disparities between estimated values and the reference values. In comparison to the methodology proposed by Hu et al. (2016) and Wang et al. (2022b), this updated approach further accounted for the spatial variability of temperature anomalies caused by day-to-day weather changes, which is more advantageous for refining LST with more spatial details. Despite the progress made, it remains challenging to fully eliminate the impact of weather variability on LST variations in the foreseeable future (Fu and Weng, 2016). Meanwhile, the results from in-situ validation have also indicated the effectiveness and feasibility of the proposed method, as evidenced by the strong correlation between the estimated values and the reference values. In addition, as the first effort to utilize multi-angle ECOSTRESS observations for investigating urban thermal anisotropies by LCZs, this study employed a space-for-time substitution approach to derive representative anisotropic profiles for different LCZs. Following a rigorous LCZ optimization process (Fig. S9), the analysis was restricted to retaining only the LCZ classes with a sufficiently large number of pixels (Ermida et al., 2017). To reduce the inherent LST retrieval and observational noise, the anisotropic profiles for LCZs generated in this study were derived through spatial aggregation. A total of 11,934 LCZ 3 pixels, 2463 LCZ 6 pixels, 1325 LCZ 9 pixels, 1483 LCZ 10 pixels, 10,594 LCZ C pixels, and 1601 LCZ D pixels were utilized to ensure a robust statistical representation of the anisotropic characteristics.

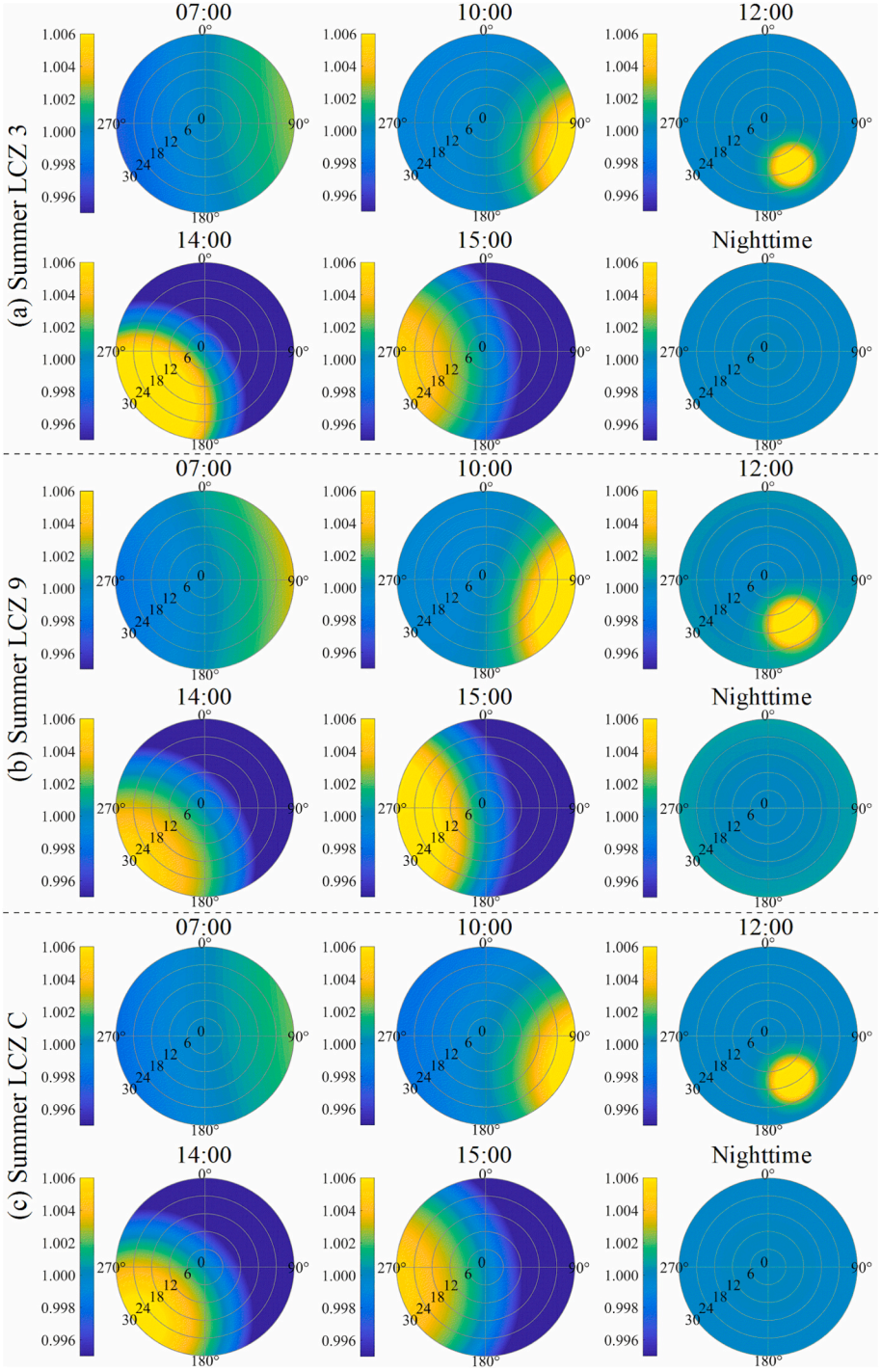


**Fig. 11.** Polar diagrams of the simulated LST anisotropic patterns for different LCZs at varying times of day in summer based on the Vinnikov-RL model: (a) LCZ 3, (b) LCZ 9, and (c) LCZ C.

### *5.2. New insights into fine-scale urban thermal anisotropies within local climate zones*

The findings yielded fresh insights into the spatial and temporal variations of anisotropy in satellite-based LST observations. By analyzing four years of data, we elucidated the angular patterns of the ECOSTRESS product, characterized by more pronounced variations in VAA compared to the VZA. Contrasting with prior studies based on observations from geostationary and polar-orbiting satellites, the findings of this study depended on a broader range of azimuth angle samples, thereby enhancing the understanding of how variations in VAA affected urban LST measurements (Ermida et al., 2017; Wang et al., 2022b). The direct evaluation of the adjusted multi-angle ECOSTRESS LST revealed that VAA variations can lead to large disparities in LST measurements. During summer midday, these differences could result in an average regional LST error of about 3.0 K, whereas in winter, the impact was smaller, approximately 1.2 K. Similar influences have been observed in previous studies utilizing UAV measurements, but have not been captured in most satellite-based research (Jiang et al., 2022; Lagouarde et al., 2012). We found that the city-scale $Max_{diff}$ in Phoenix exhibited distinct diurnal and seasonal patterns, with daytime values exceeding nighttime values, winter values exceeding summer values,

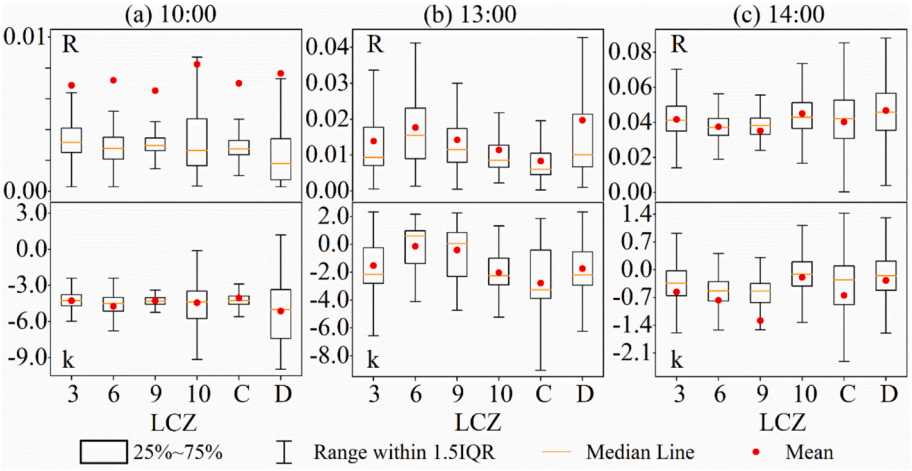


**Fig. 12.** Boxplots of the Parameter *R* and *k* for different LCZs at 10:00 (a), 13:00 (b), and 14:00 (c) in winter.

and nighttime values remaining relatively consistent. These findings are comparable to previous studies based on experimental data or satellite observations (Lagouarde et al., 2010; Wang et al., 2022b). The seasonal difference in $Max_{diff}$, with winter values exceeding summer values, arises from the combined effects of urban surface characteristics and sun-surface-sensor geometries (Ermida et al., 2017). The larger nighttime differences in seasonal $Max_{diff}$ can be attributed to the significant variations in urban surface features (e.g., vegetation cover) between summer and winter. More importantly, we generated LCZ-scale anisotropy profiles with a 200-m spatial resolution, which was a delightful advancement towards the practical application of urban thermal anisotropy research. Currently, the detailed assessment of urban heat stress increasingly relies on the integration of high-resolution multi-source remote sensing data (e.g., airborne data, ECOSTRESS, Landsat, and foreseen TRISHNA) to inform urban planning strategies targeting future global warming (Lyu et al., 2023; Xia et al., 2022). Meanwhile, LCZ serves as an effective approach for deconstructing urban heterogeneity and is generally a fundamental unit in existing urban climate studies (Huang et al., 2023; Stewart and Oke, 2012). The anisotropic profiles for LCZs can contribute to the harmonization of multi-source LST data and the development of urban 3-D LST datasets, enabling more accurate explorations of building energy demands and the heat risks in cities (Stewart et al., 2021; Yang et al., 2023). For example, Yang et al.'s (2020) study focused on estimating the complete surface temperature from nadir-viewing Landsat and ASTER observations by a semi-empirical model. Although the methodologies differ, these two studies share the same goal of optimizing the use of space-borne LST observations for various scientific inquiries. In conjunction with the semi-empirical model proposed by Yang et al. (2020), further research can explore the diurnal variations of complete surface temperature and urban surface energy exchange in diverse urban structures by attempting the nadir correction of ECOSTRESS observations using the LCZ-scale anisotropic profiles generated in this study. Furthermore, the validation results based on Landsat data can also support this point. The results suggested that after angular correction, the thermal information provided by Landsat and ECOSTRESS demonstrated enhanced comparability, allowing for their joint utilization.

In addition, the findings unveiled diurnal and seasonal variations in the anisotropic characteristics exhibited by various LCZs. The thermal contrast between surface components is the primary driver of LST anisotropy (Voogt and Oke, 2003). During summer, LCZ 6, 9, and D generally exhibited higher anisotropy compared to other LCZ types (i.e., LCZ 3, 10, and C), characterized by more pronounced hotspot intensity and width. This can be partly attributed to the relatively higher heterogeneity in surface structures, where the mixture of buildings and vegetation exacerbates temperature differences among components under varying environmental conditions (Bian et al., 2021; Hu and Wendel, 2019). The daytime anisotropy of different LCZs was typically more obvious in the winter than in summer, especially for LCZ 3 and LCZ 10. These regions had higher proportion of impervious surfaces and walls compared to other classes, and the warming effect of solar radiation on these surfaces was more evident in the winter, leading to larger component temperature differences and, consequently, greater anisotropy (Krayenhoff and Voogt, 2016; Morrison et al., 2023). The notable disparities in hot/cold spot intensity and range among various building structures also encourage more extensive investigation of thermal anisotropy across diverse underlying surfaces to enhance the interpretation and application of LST data (Qin et al., 2023). The anisotropic features of LCZ 1 and 4, characterized by high-rise buildings, were not analyzed in this study due to the rigorous optimization process applied to LCZs. Our near future research endeavors will also pay attention to high-rise buildings, for which there may be two distinct approaches to generate the corresponding thermal anisotropic profiles: 1) the synergistic utilization of multi-source remote sensing data, including MODIS, Landsat, ASTER, and ECOSTRESS, and 2) the integration of UAV experiments with ECOSTRESS observation. Furthermore, we will explore variations in LCZ-scale LST anisotropy patterns and their driving mechanism in cities under varying climatic zones and with diverse terrain and land cover conditions. We have applied the methodology proposed in this study to Salt Lake County, Utah, where the predominant LCZ types are LCZ 6, LCZ 9, LCZ A, LCZ C, and LCZ F, and the relevant results are presented in Fig. S10 – Fig. S17 and Table S4 in appendix. This exploration supports the great potential of our methodology for application in regions with a considerable number of available ECOSTRESS LST observations.

### 5.3. *Implications for the operational use of parametric models in LST angular normalization*

This study has implications for the operational use of the three-parameter Vinnikov and four-parameter Vinnikov-RL models in the angular normalization of satellite LST products. Due to the lack of multi-angle satellite observations, previous evaluations of kernel-driven models at a fine scale mostly relied on computer-simulated multi-angle LST data for simplified urban landscapes (Jiang et al., 2021). Evidently, these simplifications limited their capability in representing the complexity of real-world urban texture (e.g., building 3-D structure, material, and roughness) and the corresponding impacts on surface temperature (Wang et al., 2022a). The Vinnikov-RL model, proposed by Ermida et al. in 2018, is a new model that combines the Vinnikov and RL models. Specifically, it replaces the solar kernel of the Vinnikov model with the RL hotspot model. Such a combination serves the purpose of

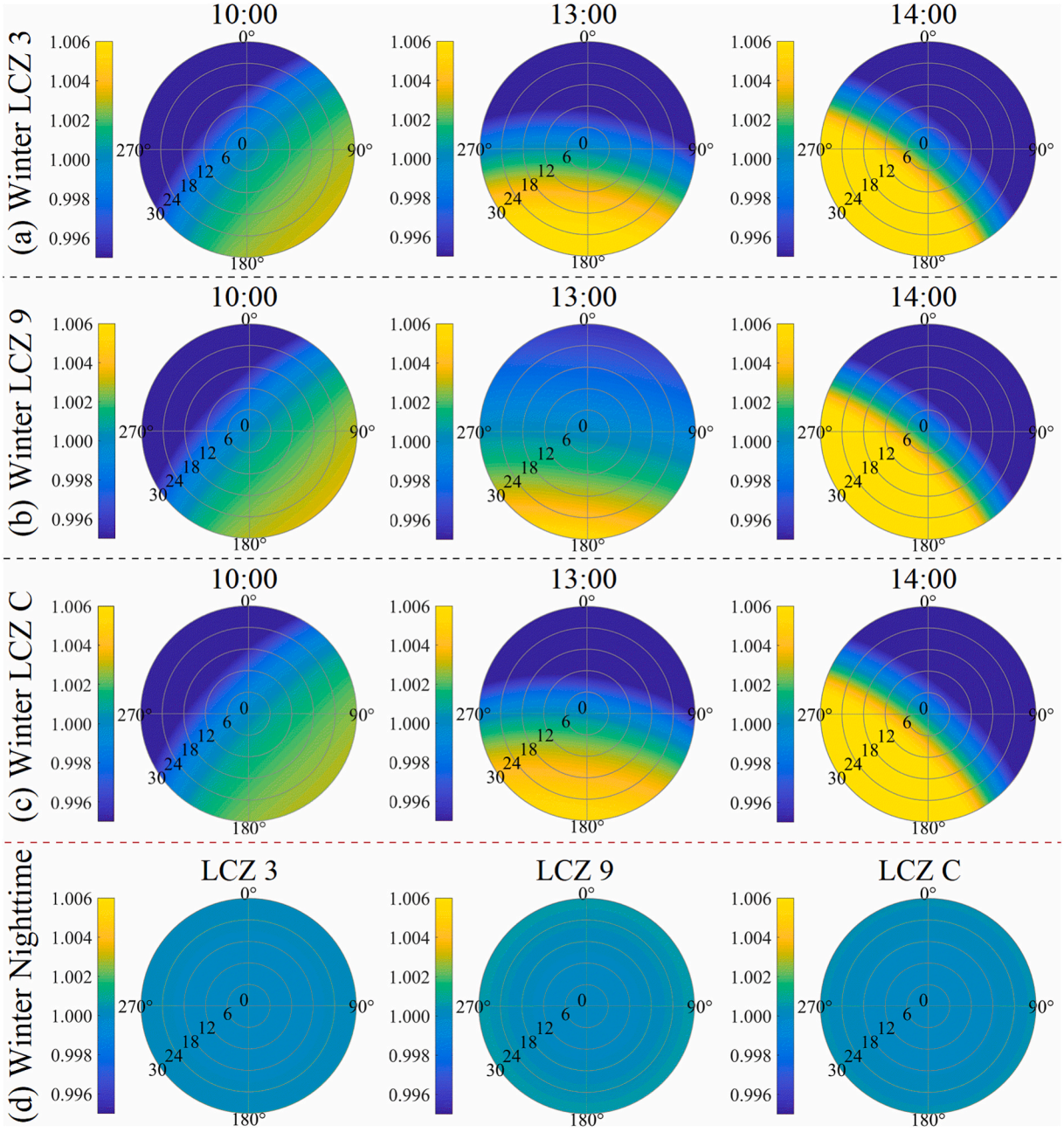


**Fig. 13.** Polar diagrams of the simulated LST anisotropic patterns for different LCZs at varying diurnal times in winter based on the Vinnikov-RL model.

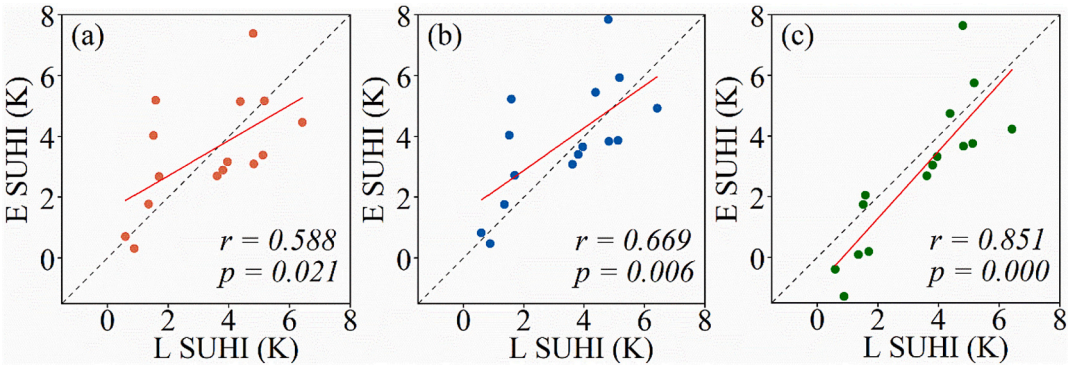


**Fig. 14.** Correlations of Landsat based SUHI to original ECOSTRESS SUHI (a), Vinnikov model corrected ECOSTRESS SUHI (b), and Vinnikov-RL model corrected ECOSTRESS SUHI (c).

integrating the strengths of both models or overcoming the respective limitations of each. However, as stated by the authors, the Vinnikov-RL model should not be simply regarded as an improved version of the Vinnikov or RL model, but rather as a modified variant of it. Their validation results merely suggest that the Vinnikov-RL model can reliably correct the directionality of LST with high quality, particularly showing improvements in performance for low tree densities and during nighttime. Consequently, Cao et al. (2021) and Jiang et al. (2021) conducted further tests using computer simulation datasets and MODIS datasets to evaluate different models' performance in different scenarios. However, it is evident that the comparisons have only been conducted under a few specific scenarios, with limited representation of urban surfaces and observational times. This study assessed the performance of two models in correcting angular effects in urban areas using nadir observations from Landsat. The results suggested that both models could effectively correct multi-angle observations from ECOSTRESS, achieving a satisfactory level of consistency with the nadir observations. Notably, the Vinnikov-RL model outperformed the Vinnikov model, which is attributed to its explicit consideration of the hotspot effect.

This study presented the initial attempt to statistically quantify the coefficients of two representative kernel-driven models for 200-m LCZs within a large spatial extent. Such exploration should be a necessary step before the operational use of kernel-driven models in satellite LST products, while also advocating for more research on the anisotropy of actual underlying surfaces at the satellite observational scales (Cao et al., 2019). The findings revealed obvious variations in the parameters derived from the Vinnikov model among different LCZs but good consistency within the same LCZ. This partly underscored the robust performance of the linear Vinnikov model in fitting these irregularly distributed ECOSTRESS observations (Ermida et al., 2017). The nonlinear Vinnikov-RL model appeared to impose a higher demand for the configuration of observation angles when calibrating model parameters (Ran et al., 2022). Therefore, despite obtaining multi-angle observations at different times of the day, we could only achieve satisfactory fitting results for a limited number of time points. Moreover, the distribution of fitted parameters across different LCZs was not as smooth as that of the Vinnikov model. On the other hand, the visualized simulation results also supported the point that the Vinnikov-RL model, by virtue of its intrinsic design, outperformed the Vinnikov model in effectively capturing hotspot effects, while allowing for the adjustment of its parameters $\Delta T_{HS}$ and $k$ within the diurnal cycle (Cao et al., 2021; Ermida et al., 2018). Overall, while the validation results also indicated the better correlation performance of the Vinnikov-RL model compared to the Vinnikov model, the Vinnikov model remains a viable and convincing option in many situations.

### 5.4. Limitations

Some limitations and uncertainties in the analyses deserve to be noted. First, the multi-angle ECOSTRESS LST observations were acquired on different days with varying weather and atmospheric conditions. In this study, aided by GOES-R LST and in-situ air temperature data, we generated a quasi-simultaneous multi-angle ECOSTRESS LST dataset by minimizing the impacts of weather-related and diurnal LST variations. However, given the high spatiotemporal heterogeneity of LST, this approach may not entirely dissolve uncertainties. Second, limitations exist when simulating LST anisotropy using ECOSTRESS observations. Due to the constraints of sensor VZA, the simulated LCZ-scale results only reflect LST anisotropy situations within a VZA of 30°. Owing to the limited ECOSTRESS samples, the findings can only provide statistical profiles of LCZ-scale LST anisotropy aggregated over time. Besides, only three pairs of Landsat/ECOSTRESS images were available for model performance assessment. Given the dependence of kernel models on sampling angles, further research will prioritize the integration of UAV-based observations to enable more context-specific validation, thereby improving the calibration of urban LST anisotropy at finer spatiotemporal scales. The future availability of a longer ECOSTRESS record will also alleviate these limitations. Third, this study only shows LST anisotropic patterns of six LCZ types and the performance of two representative kernel-driven models. Benefiting from the global high-frequency sampling capability of ECOSTRESS, we will extend our research to other regions with diverse underlying surfaces, where there are more available ECOSTRESS observations and additional high-resolution multi-angle remotely sensed LST data.

## 6. Conclusions

Given the ongoing acquisition of thermal observations from space, understanding LST anisotropy becomes crucial not only for ensuring the accurate interpretation of LST observations and comparability of multi-source LST products but also for enhancing confidence in their practical applications. This study utilized multi-angle LST observations from ECOSTRESS to investigate the seasonal and diurnal variations of urban thermal anisotropy at both the city and 200-m LCZ scales in Phoenix City, Arizona. Our findings revealed that ECOSTRESS observations manifested unique angular patterns, featuring substantial variations in VAA and limited changes in VZA within a 30° range. An effective method was developed to generate the quasi-simultaneous multi-angle ECOSTRESS LST dataset for each hour of the day (i.e., a 24-h period) in summer and winter. Based on this dataset, Vinnikov and Vinnikov-RL models were employed to assess the angular effect on LST measurements. The results demonstrated that angular effect led to notable variations in the observed LST, with potential deviations at the city scale of up to 10 K during winter and around 5 K during summer relative to the nadir LST. Furthermore, our findings suggested that LST anisotropy exhibited distinct diurnal and seasonal patterns across LCZs, characterized by prominent variations in intensity and width of hot/cold spots. In both summer and winter, LCZ 6, 9, and D usually displayed higher hotspot intensity and width than other LCZs at varying times of day. During nighttime, the directional signal of LST was not prominent and could be ignored. The generated LCZ-scale anisotropy profiles can support the angular correction of multi-source LST observations. Additionally, the validation results showed that the Vinnikov-RL model had good performance in accurately simulating diurnal LST anisotropy over LCZs. Our study highlights the potential of multi-angle ECOSTRESS LST observations for exploring urban thermal anisotropy. Future research will prioritize the integration of ECOSTRESS observations with other remotely sensed LST measurements (e.g., airborne, Landsat, MODIS, and foreseen TRISHNA data) to generate comprehensive urban thermal anisotropy profiles globally at different spatial and temporal scales. Besides, efforts will be made to harmonize multi-source LST data to improve urban climate research.

## CRediT authorship contribution statement

**Yue Chang:** Writing – original draft, Methodology, Investigation, Formal analysis, Data curation, Conceptualization. **Qihao Weng:** Writing – review & editing, Supervision, Methodology, Investigation, Funding acquisition, Formal analysis, Conceptualization. **James A. Voogt:** Writing – review & editing, Methodology, Investigation, Formal analysis. **Jingfeng Xiao:** Writing – review & editing, Investigation, Formal analysis.

## Declaration of competing interest

We declare that we have no known competing financial interests or personal relationships that could have appeared to influence the work reported in this paper.

## Acknowledgements

We thank the three anonymous reviewers for their constructive and

insightful comments on our manuscript. This research has received funding from Global STEM Professorship, Hong Kong SAR Government (P0039329), Hong Kong RGC GRF (15300923), and Hong Kong Polytechnic University (P0046482, P0038446, and P0042484).

## Appendix A. Supplementary data

Supplementary data to this article can be found online at https://doi.org/10.1016/j.rse.2025.114705.

## Data availability

Data will be made available on request.

## References

Bian, Z., Cao, B., Li, H., Du, Y., Lagouarde, J.-P., Xiao, Q., Liu, Q., 2018. An analytical four-component directional brightness temperature model for crop and forest canopies. Remote Sens. Environ. 209, 731–746.
Bian, Z., Roujean, J.-L., Cao, B., Du, Y., Li, H., Gamet, P., Fang, J., Xiao, Q., Liu, Q., 2021. Modeling the directional anisotropy of fine-scale TIR emissions over tree and crop canopies based on UAV measurements. Remote Sens. Environ. 252, 112150.
Brandi, A., Martilli, A., Salamanca, F., Georgescu, M., 2024. Urban boundary-layer flows in complex terrain: Dynamic interactions during a hot and dry summer season in Phoenix, Arizona. Q. J. R. Meteorol. Soc. 150 (762), 3099–3116. July 2024 Part A.
Cao, B., Liu, Q., Du, Y., Roujean, J.-L., Gastellu-Etchegorry, J.P., Trigo, I.F., Zhan, W., Yu, Y., Cheng, J., Jacob, F., Lagouarde, J.-P., Bian, Z., Li, H., Hu, T., Xiao, Q., 2019. A review of earth surface thermal radiation directionality observing and modeling: historical development, current status and perspectives. Remote Sens. Environ. 232, 111304.
Cao, B., Roujean, J.L., Gastellu-Etchegorry, J.P., Liu, Q., Du, Y., Lagouarde, J.P., Huang, H., Li, H., Bian, Z., Hu, T., Qin, B., Ran, X., Xiao, Q., 2021. A general framework of kernel-driven modeling in the thermal infrared domain. Remote Sens. Environ. 252, 112157.
Chang, Y., Xiao, J., Li, X., Middel, A., Zhang, Y., Gu, Z., Wu, Y., He, S., 2021. Exploring diurnal thermal variations in urban local climate zones with ECOSTRESS land surface temperature data. Remote Sens. Environ. 263, 112544.
Chang, Y., Xiao, J., Li, X., Weng, Q., 2023. Monitoring diurnal dynamics of surface urban heat island for urban agglomerations using ECOSTRESS land surface temperature observations. Sustain. Cities Soc. 98, 104833.
Coll, C., Galve, J.M., Niclòs, R., Valor, E., Barberà, M.J., 2019. Angular variations of brightness surface temperatures derived from dual-view measurements of the advanced along-track scanning radiometer using a new single band atmospheric correction method. Remote Sens. Environ. 223, 274–290.
Connors, J.P., Galletti, C.S., Chow, W.T.L., 2012. Landscape configuration and urban heat island effects: assessing the relationship between landscape characteristics and land surface temperature in Phoenix, Arizona. Landsc. Ecol. 28, 271–283.
Demuzere, M., Kittner, J., Bechtel, B., 2021. LCZ generator: a web application to create local climate zone maps. Front. Environ. Sci. 9, 637455.
Du, H., Zhan, W., Liu, Z., Scott Krayenhoff, E., Chakraborty, T.C., Zhao, L., Jiang, L., Dong, P., Li, L., Huang, F., Wang, S., Xu, Y., 2023. Global mapping of urban thermal anisotropy reveals substantial potential biases for remotely sensed urban climates. Sci. Bull. 68 (16), 1809–1818.
Duffour, C., Olioso, A., Demarty, J., Van der Tol, C., Lagouarde, J.P., 2015. An evaluation of SCOPE: a tool to simulate the directional anisotropy of satellite-measured surface temperatures. Remote Sens. Environ. 158, 362–375.
Duffour, C., Lagouarde, J.P., Roujean, J.L., 2016. A two parameter model to simulate thermal infrared directional effects for remote sensing applications. Remote Sens. Environ. 186, 250–261.
Ermida, S.L., DaCamara, C.C., Trigo, I.F., Pires, A.C., Ghent, D., Remedios, J., 2017. Modelling directional effects on remotely sensed land surface temperature. Remote Sens. Environ. 190, 56–69.
Ermida, S.L., Trigo, I.F., DaCamara, C.C., Roujean, J.-L., 2018. Assessing the potential of parametric models to correct directional effects on local to global remotely sensed LST. Remote Sens. Environ. 209, 410–422.
Fu, P., Weng, Q., 2016. A time series analysis of urbanization induced land use and land cover change and its impact on land surface temperature with Landsat imagery. Remote Sens. Environ. 175, 205–214.
Fu, P., Xie, Y., Weng, Q., Myint, S., Meacham-Hensold, K., Bernacchi, C., 2019. A physical model-based method for retrieving urban land surface temperatures under cloudy conditions. Remote Sens. Environ. 230, 111191.
Guillevic, P.C., Bork-Unkelbach, A., Gottsche, F.M., Hulley, G., Gastellu-Etchegorry, J.-P., Olesen, F.S., Privette, J.L., 2013. Directional viewing effects on satellite land surface temperature products over sparse vegetation canopies - a multisensor analysis. IEEE Geosci. Remote Sens. Lett. 10 (6), 1464–1468.
Guo, M., Cao, B., Fan, W., Ren, H., Cui, Y., Du, Y., Liu, Q., 2019. Scattering effect contributions to the directional canopy emissivity and brightness temperature based on CE-P and CBT-P models. IEEE Geosci. Remote Sens. Lett. 16 (6), 957–961.
Hook, S.J., Cawse-Nicholson, K., Barsi, J., Radocinski, R., Hulley, G.C., Johnson, W.R., Rivera, G., Markham, B., 2020. In-flight validation of the ECOSTRESS, Landsats 7 and 8 thermal infrared spectral channels using the Lake Tahoe CA/NV and Salton Sea CA automated validation sites. IEEE Trans. Geosci. Remote Sens. 58 (2), 1294–1302.
Hu, L., Wendel, J., 2019. Analysis of urban surface morphologic effects on diurnal thermal directional anisotropy. ISPRS J. Photogramm. Remote Sens. 148, 1–12.
Hu, L., Monaghan, A., Voogt, J.A., Barlage, M., 2016. A first satellite-based observational assessment of urban thermal anisotropy. Remote Sens. Environ. 181, 111–121.
Hu, T., Roujean, J.-L., Cao, B., Mallick, K., Boulet, G., Li, H., Xu, Z., Du, Y., Liu, Q., 2023. Correction for LST directionality impact on the estimation of surface upwelling longwave radiation over vegetated surfaces at the satellite scale. Remote Sens. Environ. 295, 113649.
Huang, F., Jiang, S., Zhan, W., Bechtel, B., Liu, Z., Demuzere, M., Huang, Y., Xu, Y., Ma, L., Xia, W., Quan, J., Jiang, L., Lai, J., Wang, C., Kong, F., Du, H., Miao, S., Chen, Y., Chen, J., 2023. Mapping local climate zones for cities: a large review. Remote Sens. Environ. 292, 113573.
Hulley, G., Shivers, S., Wetherley, E., Cudd, R., 2019. New ECOSTRESS and MODIS land surface temperature data reveal fine-scale heat vulnerability in cities: a case study for Los Angeles County, California. Remote Sens. 11 (18), 2136.
Hulley, G.C., Göttsche, F.M., Rivera, G., Hook, S.J., Freepartner, R.J., Martin, M.A., Cawse-Nicholson, K., Johnson, W.R., 2021. Validation and quality assessment of the ECOSTRESS level-2 land surface temperature and emissivity product. IEEE Trans. Geosci. Remote Sens. 60, 1–23.
Jiang, L., Zhan, W., Hu, L., Huang, F., Hong, F., Liu, Z., Lai, J., Wang, C., 2021. Assessment of different kernel-driven models for daytime urban thermal radiation directionality simulation. Remote Sens. Environ. 263, 112562.
Jiang, L., Zhan, W., Tu, L., Dong, P., Wang, S., Li, L., Wang, C., Wang, C., 2022. Diurnal variations in directional brightness temperature over urban areas through a multi-angle UAV experiment. Build. Environ. 222, 109408.
Jiao, W., Wang, L., McCabe, M.F., 2021. Multi-sensor remote sensing for drought characterization: current status, opportunities and a roadmap for the future. Remote Sens. Environ. 256, 112313.
Krayenhoff, E.S., Voogt, J.A., 2016. Daytime thermal anisotropy of urban neighborhoods: morphological causation. Remote Sens. 8 (2), 108.
Lagouarde, J.P., Irvine, M., 2008. Directional anisotropy in thermal infrared measurements over Toulouse city Centre during the CAPITOUL measurement campaigns: first results. Meteorog. Atmos. Phys. 102 (3–4), 173–185.
Lagouarde, J.P., Hénon, A., Kurz, B., Moreau, P., Irvine, M., Voogt, J., Mestayer, P., 2010. Modelling daytime thermal infrared directional anisotropy over Toulouse city Centre. Remote Sens. Environ. 114 (1), 87–105.
Lagouarde, J.P., Hénon, A., Irvine, M., Voogt, J., Pigeon, G., Moreau, P., Masson, V., Mestayer, P., 2012. Experimental characterization and modelling of the nighttime directional anisotropy of thermal infrared measurements over an urban area: case study of Toulouse (France). Remote Sens. Environ. 117, 19–33.
Li, Z.L., Wu, H., Duan, S.B., Zhao, W., Ren, H., Liu, X., Leng, P., Tang, R., Ye, X., Zhu, J., Sun, Y., Si, M., Liu, M., Li, J., Zhang, X., Shang, G., Tang, B.H., Yan, G., Zhou, C., 2023. Satellite remote sensing of global land surface temperature: definition, methods, products, and applications. Rev. Geophys. 61 (1), e2022RG000777.
Logan, T.M., Zaitchik, B., Guikema, S., Nisbet, A., 2020. Night and day: the influence and relative importance of urban characteristics on remotely sensed land surface temperature. Remote Sens. Environ. 247, 111861.
Lyu, R., Pang, J., Tian, X., Zhao, W., Zhang, J., 2023. How to optimize the 2D/3D urban thermal environment: insights derived from UAV LiDAR/multispectral data and multi-source remote sensing data. Sustain. Cities Soc. 88, 104287.
Manoli, G., Fatichi, S., Bou-Zeid, E., Katul, G.G., 2020. Seasonal hysteresis of surface urban heat islands. Proc. Natl. Acad. Sci. 117 (13), 7082–7089.
Morrison, W., Grimmond, S., Kotthaus, S., 2023. Simulating satellite urban land surface temperatures: sensitivity to sensor view angle and assumed landscape complexity. Remote Sens. Environ. 293, 113579.
Qin, B., Cao, B., Roujean, J.-L., Gastellu-Etchegorry, J.P., Ermida, S.L., Bian, Z., Du, Y., Hu, T., Li, H., Xiao, Q., Chen, S., Liu, Q., 2023. A thermal radiation directionality correction method for the surface upward longwave radiation of geostationary satellite based on a time-evolving kernel-driven model. Remote Sens. Environ. 294, 113599.
Ran, X., Cao, B., Qin, B., Bian, Z., Du, Y., Li, H., Xiao, Q., Liu, Q., 2022. Assessment of five thermal infrared kernel-driven models using limited multiangle observations. IEEE Geosci. Remote Sens. Lett. 19, 1–5.
Rasmussen, M.O., Gottsche, F.-M., Olesen, F.-S., Sandholt, I., 2011. Directional effects on land surface temperature estimation from Meteosat second generation for savanna landscapes. IEEE Trans. Geosci. Remote Sens. 49, 4458–4468.
Roujean, J.L., 2000. A parametric hot spot model for optical remote sensing applications. Remote Sens. Environ. 71 (2), 197–206.
Schwaab, J., Meier, R., Mussetti, G., Seneviratne, S., Burgi, C., Davin, E.L., 2021. The role of urban trees in reducing land surface temperatures in European cities. Nat. Commun. 12 (1), 6763.
Stewart, I.D., Oke, T.R., 2012. Local climate zones for urban temperature studies. Bull. Am. Meteorol. Soc. 93 (12), 1879–1900.
Stewart, I.D., Krayenhoff, E.S., Voogt, J.A., Lachapelle, J.A., Allen, M.A., Broadbent, A. M., 2021. Time evolution of the surface urban heat island. Earth. Future 9 (10), e2021EF002178.
Su, Y., Zhang, C., Ciais, P., Zeng, Z., Cescatti, A., Shang, J., Chen, J.M., Liu, J., Wang, Y. P., Yuan, W., Peng, S., Lee, X., Zhu, Z., Fan, L., Liu, X., Liu, L., Lafortezza, R., Li, Y., Ren, J., Yang, X., Chen, X., 2023. Asymmetric influence of forest cover gain and loss on land surface temperature. Nat. Clim. Chang. 13 (8), 823–831.
Vinnikov, K.Y., Yu, Y., Rama Varma Raja, M.K., Tarpley, D., Goldberg, M.D., 2008. Diurnal-seasonal and weather-related variations of land surface temperature observed from geostationary satellites. Geophys. Res. Lett. 35 (22).

Vinnikov, K.Y., Yu, Y., Goldberg, M.D., Chen, M., Tarpley, D., 2011. Scales of temporal and spatial variability of midlatitude land surface temperature. J. Geophys. Res.-Atmos. 116 (D2).
Vinnikov, K.Y., Yu, Y., Goldberg, M.D., Tarpley, D., Romanov, P., Laszlo, I., Chen, M., 2012. Angular anisotropy of satellite observations of land surface temperature. Geophys. Res. Lett. 39 (23).
Voogt, J.A., 2008. Assessment of an urban sensor view model for thermal anisotropy. Remote Sens. Environ. 112 (2), 482–495.
Voogt, J.A., Oke, T.R., 1998. Effects of urban surface geometry on remotely-sensed surface temperature. Int. J. Remote Sens. 19 (5), 895–920.
Voogt, J.A., Oke, T.R., 2003. Thermal remote sensing of urban climates. Remote Sens. Environ. 86 (3), 370–384.
Wang, D., Chen, Y., Hu, L., Voogt, J.A., Gastellu-Etchegorry, J.-P., Krayenhoff, E.S., 2021. Modeling the angular effect of MODIS LST in urban areas: a case study of Toulouse, France. Remote Sens. Environ. 257, 112361.
Wang, D., Chen, Y., Hu, L., Voogt, J.A., 2022a. Urban thermal anisotropy: a comparison among observational and modeling approaches at different time scales. IEEE Trans. Geosci. Remote Sens. 60, 1–15.
Wang, D., Chen, Y., Hu, L., Voogt, J.A., He, X., 2022b. Satellite-based daytime urban thermal anisotropy: a comparison of 25 global cities. Remote Sens. Environ. 283, 113312.
Wang, J., Tang, R., Jiang, Y., Liu, M., Li, Z.-L., 2023. A practical method for angular normalization of global MODIS land surface temperature over vegetated surfaces. ISPRS J. Photogramm. Remote Sens. 199, 289–304.
Weng, Q., 2009. Thermal infrared remote sensing for urban climate and environmental studies: methods, applications, and trends. ISPRS J. Photogramm. Remote Sens. 64 (4), 335–344.
Wooster, M.J., Roberts, G.J., Giglio, L., Roy, D.P., Freeborn, P.H., Boschetti, L., Justice, C., Ichoku, C., Schroeder, W., Davies, D., Smith, A.M.S., Setzer, A., Csiszar, I., Strydom, T., Frost, P., Zhang, T., Xu, W., de Jong, M.C., Johnston, J.M., Ellison, L., Vadrevu, K., Sparks, A.M., Nguyen, H., McCarty, J., Tanpipat, V., Schmidt, C., San-Miguel-Ayanz, J., 2021. Satellite remote sensing of active fires: history and current status, applications and future requirements. Remote Sens. Environ. 267, 112694.
Xia, H., Chen, Y., Song, C., Li, J., Quan, J., Zhou, G., 2022. Analysis of surface urban heat islands based on local climate zones via spatiotemporally enhanced land surface temperature. Remote Sens. Environ. 273, 112972.
Yang, J., Wong, M.S., Ho, H.C., Krayenhoff, E.S., Chan, P.W., Abbas, S., Menenti, M., 2020. A semi-empirical method for estimating complete surface temperature from radiometric surface temperature, a study in Hong Kong city. Remote Sens. Environ. 237, 111540.
Yang, J., Wu, Z., Menenti, M., Wong, M.S., Xie, Y., Zhu, R., Abbas, S., Xu, Y., 2023. Impacts of urban morphology on sensible heat flux and net radiation exchange. Urban Clim. 50, 101588.
Yu, Y., Yu, P., 2020. Land surface temperature product from the GOES-R series. In: The GOES-R Series. Elsevier, pp. 133–144.